Dihydroceramide desaturase governs endoplasmic reticulum and lipid droplet homeostasis to promote glial function in the nervous system

Yuqing Zhu[1], Kevin Cho[2,3,4], Haluk Lacin[5], Yi Zhu[1], Jose DiPaola[1], Beth A. Wilson[1], Gary J. Patti[2,3,4], James B. Skeath[1]

[1]Department of Genetics, Washington University School of Medicine, 4523 Clayton Avenue, St. Louis, MO 63110, USA

[2]Department of Chemistry, Washington University in St. Louis, One Brookings Drive, St. Louis, MO 63130, USA

[3]Department of Medicine, Washington University School of Medicine, St. Louis, MO 63110, USA

[4]Center for Proteomics, Metabolomics, and Isotope Tracing, Washington University in St. Louis, One Brookings Drive, St. Louis, MO 63130, USA

[5]Division of Biological and Biomedical Systems, University of Missouri-Kansas City, Kansas City, MO 64110, USA

Key words: *DEGS1*, *ifc*, ceramide, glia, lipid droplet, endoplasmic reticulum, leukodystrophy, CNS development, sphingolipids

ABSTRACT

Dihydroceramide desaturases convert dihydroceramides to ceramides in the last step of the *de novo* ceramide pathway. Reduction of DEGS1 dihydroceramide desaturase function in humans leads to the rare neurodegenerative disorder hypomyelinating leukodystrophy-18, but the exact mechanism that underlies the disease remains unclear. Through a forward genetic screen, we discovered that *infertile crescent (ifc)*, the sole *Drosophila* dihydroceramide desaturase, governs central nervous system development and morphology. Expressed and genetically active most prominently in glia rather than neurons, *ifc* primarily controls nervous system development through a cell autonomous function in glia. Within the nervous system, loss of *ifc* results in ceramide depletion, dihydroceramide accumulation, and increased saturation of major membrane phospholipids. At the cellular level, loss of *ifc* leads to severe glial defects, particularly in cortex glia, including expansion of the endoplasmic reticulum, cell swelling, failure to enwrap neurons, and lipid droplet depletion. Our research supports a model in which inappropriate retention of dihydroceramide in the endoplasmic reticulum (ER) of glial cells drives ER expansion and cell swelling, disrupting glial function and leading to subsequent nervous system dysfunction. Given the conserved nature of the *de novo* ceramide biosynthesis pathway, our findings in the fly system suggest that dihydroceramide-triggered expansion of the ER in the membrane-rich glial cells may be the proximal cause of hypomyelinating leukodystrophy-18 in humans.

INTRODUCTION

Key structural and functional components of the cell membrane in all eukaryotic cells, sphingolipids are enriched in glial cells, such as oligodendrocytes, where they comprise up to 30% of all membrane lipids (Jackman et al., 2009). Complex sphingolipids, like glycosylsphingolipids and sphingomyelin, derive from ceramide (Ghosh et al., 2013; Vacaru et al., 2013; Hannun & Obeid, 2018). In the de novo ceramide biosynthesis pathway, dihydroceramide desaturases, such as human DEGS1, produce ceramide from dihydroceramide by catalyzing the formation of a *trans* double bond between carbons 4 and 5 of the sphingoid backbone, which enhances its conformational plasticity (Li et al., 2002; Al Sazzad and Slotte, 2016). In humans, bi-allelic mutations in *DEGS1* cause hypomyelinating leukodystrophy-18 (HLD-18), a progressive, often fatal pediatric neurodegenerative disease marked by cerebral atrophy, white matter reduction, and hypomyelination (Dolgin et al., 2019; Karsai et al., 2019; Pant et al.,2019). The primary cell type impacted by loss of *DEGS1* function in the nervous system and the cell biology of how disruption of ceramide synthesis leads to neurodegeneration and myelination defects remain unknown.

A hotspot for human neurodegenerative disease, the sphingolipid metabolic pathway is well conserved in higher metazoans (Fryst et al., 2004; Acharya & Acharya, 2005; Hannun & Obeid, 2018; Dunn et al., 2019; Pan et al., 2023). *De novo* ceramide synthesis occurs in the endoplasmic reticulum (ER) and starts with the rate-limiting condensation of serine and palmitoyl-CoA (or lauoryl-CoA in flies) by the serine palmitoyltransferase (SPT) complex to form 3-Ketosphinganine, which is converted to sphinganine by 3-Ketosphinganine reductase. Ceramide synthases condense sphinganine with acyl-CoA to generate dihydroceramide, which is converted to ceramide by dihydroceramide desaturases. Ceramide is then efficiently transported by the specific ceramide transporter CERT from the ER to the Golgi (Kumagai et al., 2005), where it

undergoes different headgroup modifications to produce complex sphingolipids eventually translocate to the plasma membrane (Kobayashi & Menon, 2018).

Consistent with its central role in ceramide biogenesis, reduction or loss of *DEGS1* function in human patients or cell lines, mice, zebrafish, and flies drives dihydroceramide accumulation and ceramide depletion (Holland et al., 2007; Jung et al., 2017; Karsai et al., 2019; Pant et al., 2019). HLD-18 patients display reduced myelin sheath thickness in peripheral nerves, and knockdown of *DEGS1* function in zebrafish reduces the number of myelin basic protein-positive oligodendrocytes (Karsai et al, 2019; Pant et al., 2019), suggesting *DEGS1* regulates Schwann cell and oligodendrocyte development. In *Drosophila*, genetic ablation of *infertile crescent* (*ifc*), the fly ortholog of *DEGS1*, drives activity-dependent photoreceptor neuron degeneration (Jung et al., 2017), suggesting that *ifc* function is crucial for neuronal homeostasis. In addition, forced expression of a wild-type *ifc* transgene in neurons, glia, or muscles was shown to rescue the *ifc* mutant phenotype (Jung et al., 2017). It then remains to be determined whether *ifc/DEGS1* acts primarily in glia, neurons, or other cells to regulate nervous system development.

Research on *DEGS1* points to dihydroceramide accumulation as the major driver of nervous system defects caused by *DEGS1* deficiency. Pharmacological or genetic inhibition of ceramide synthase function, which should reduce dihydroceramide levels, suppresses the observed reduction of MBP-positive oligodendrocytes in zebrafish and the activity-dependent photoreceptor degeneration in flies triggered by reduction or loss of *DEGS1/ifc* function (Jung et al., 2017; Pant et al., 2019). Dihydroceramide accumulation may also contribute to other neurodegenerative diseases, as gain of function mutations in *SPTLC1* and *SPTLC2*, which act in the SPT complex to catalyze the initial step of ceramide synthesis, cause juvenile amyotrophic lateral sclerois due to elevated sphingolipid biosynthesis, with dihydroceramides showing the greatest relative increase of all sphingolipids (Lone et al., 2022; Lone et al., 2023; Syeda et al.,

2023; Dohrn et al., 2023). How dihydroceramide accumulation alters the cell biology of neurons, glia, or both to trigger myelination defects and neurodegeneration is unclear.

With its vast genetic toolkit, *Drosophila* has emerged as a powerful system in which to dissect the genes and pathways that regulate glial development and function (Freeman and Doherty, 2006; Coutinho-Budd and Freeman, 2013). In flies, six morphologically and functionally distinct glial subtypes regulate nervous system development and homeostasis (Yildirim et al., 2019; Corty & Coutinho-Budd, 2023). The surface perineurial and subperineural glia act as physiochemical barriers to protect the nervous system and control metabolite exchange with the hemolymph, carrying out a similar function as the human blood-brain-barrier (Stork et al., 2008; Volkenhoff et al., 2015). Residing between the surfact glia and the neuropil, cortex glia ensheath the cell bodies of neuroblasts and neurons in the CNS in protective, nutritive, honeycomb-like membrane sheaths. Ensheathing glia define the boundary of the neuropil and insulate axons, dendrites, and synapses from neuronal cell bodies in the CNS (Freeman, 2015). Astrocyte-like glia extend fine membrane protrusions that infiltrate the neuropil and form a meshwork of cellular processes that ensheath synapses and regulate synaptic homestasis in the CNS (Freeman, 2015). In the PNS, wrapping glia reside internally to the surface glia and insulate axons in the PNS to enhance neuronal signaling and to provide energy support.

Using the *Drosophila* model, we found that *ifc* primarily acts in glia to regulate CNS development with its loss disrupting the morphology of most glial subtypes during larval life. Our work supports a model in which inappropriate retention of dihydroceramide in the ER drives ER expansion, glial swelling, and the failure of glia to enwrap neurons, ultimately leading to neuronal degeneration as a secondary consequence of glial dysfunction. Given the conserved nature of *de novo* ceramide biosynthesis, our findings likely illuminate the underlying cellular and subcellular defects that disrupt nervous system development and drive neurodegeneration upon loss of *ifc/DEGS1* function in flies and humans.

RESULTS

ifc contributes to the regulation developmental timing and CNS structure

In an EMS-based forward genetic screen of the second chromosome, we uncovered three non-complementing mutations that resulted in identical phenotypes when homozygous or trans-heterozygous to each other, including a 3-day or greater delay in reaching the late-third larval instar stage, reduced brain size, progressive elongation of the ventral nerve cord, axonal swelling, and lethality at the late larval or early pupal stage (Fig. 1a; data not shown). Whole genome sequencing revealed that *ifc,* the *Drosophila* ortholog of *DEGS1,* was independently mutated in the three lines: ifc^{js1} and ifc^{js2} encode V276D and G257S missense mutations, respectively, and ifc^{js3} encodes a W162* nonsense mutation (Fig. 1a-b). Sanger sequencing also uncovered a missense mutation, E241K, in the molecularly uncharacterized ifc^{1} allele (Fig. 1b). All four mutations reside in the fatty acid desaturase domain, the hotspot for mutations in human *DEGS1* that cause HLD-18 (Fig. 1b-b').

To investigate *ifc* function, we confirmed the genetic nature of our alleles, as a prior study reported that a CRISPR-generated, gene-specific deletion of *ifc, ifc-KO,* resulted in early larval lethality (Jung et al. 2017), but our *ifc* alleles caused late larval-early pupal lethality. Complementation crosses of each *ifc* allele against a deficiency of the region (Df(2L)BSC184) and *ifc-KO* revealed that all combinations, including larvae trans-heterozygous for *ifc-KO* over Df(2L)BSC184, survived to the late larval-early pupal stage and yielded phenotypes identical to those detailed above for the newly uncovered *ifc* alleles. Flies homozygous for *ifc-KO*, however, die as early larvae. Further genetic analysis uncovered second site mutation(s) in the 21E2 chromosomal region responsible for the early larval lethal phenotype of the *ifc-KO* chromosome (see Methods). When uncoupled from these mutation(s), larvae homozygous for the “clean” *ifc-*

KO chromosome developed to the late larval-early pupal stage and manifested phenotypes identical to the new *ifc* alleles. This analysis defined the correct lethal phase of *ifc* and identified our *ifc* alleles as strong loss of function mutations.

Loss of *ifc* function drives ceramide depletion and dihydroceramide accumulation

As *ifc/DEGS1* converts dihydroceramide to ceramide, we used untargeted metabolomics on whole larvae and the isolated CNS from wild-type and *ifc-KO/ifc*^{JS3} larvae (hereafter termed *ifc*$^{-/-}$ larvae) to assess the effect of loss of *ifc* function on metabolites in the ceramide pathway (Fig. 1c). Loss of *ifc* function resulted in a near complete loss of ceramides and a commensurate increase in dihydroceramides in the CNS and whole larvae (Fig. 1e, S1). Sphinganine, the metabolite directly upstream of dihydroceramide, also exhibited a significant increase in its levels in the absence of *ifc* function, while metabolites further upstream were not detected or unchanged in abundance (Fig. 1e, S1). Ceramide derivatives like sphingosine, CPE, and Glucosyl-Ceramide (Glc-Cer), were reduced in levels and replaced by their cognate dihydroceramide forms (e.g., Glc-DiCer) (Fig. 1e, S1). The enzymatic function of Ifc is then absent in the *ifc*$^{-/-}$ mutant larvae; its loss drives dihydroceramide accumulation and ceramide loss.

***ifc* governs glial morphology and survival**

To connect this metabolic profile to a cellular phenotype, we assayed *ifc* function in the CNS. We leveraged the *M{3xP3-RFP.attP}* phi-C31 “landing pad” transgene as a general glial marker because we found that it drives RFP expression in most glial subtypes (Fig. S2), and the expression of fatty acid binding protein (FABP) as a marker of cortex glia (Kis et al., 2015). In addition, we labeled neuroblasts with Deadpan (Dpn), neurons with ELAV, and axons with N-Cadherin (NCad). In *ifc*$^{-/-}$ larvae, we observed a clear reduction in Dpn-positive neuroblasts in the

optic lobe, swelling of wrapping glia in peripheral nerves, enhanced RFP expression in the CNS, and the presence of large swollen, cortex glia identified by RFP labeling and fatty acid binding protein (FABP) expression (Fig. 1f). In wild-type larvae, cortex glia display compact cell bodies and fully enwrap individual neuronal cell bodies with their membrane sheaths (Fig. 1f, S3, S4; Kis et al., 2015). In *ifc*$^{-/-}$ larvae, cortex glia display swollen cell bodies, fail to fully enwrap neuronal cell bodies, displace neurons from their regular arrangement, and contain brightly fluorescent RFP-positive aggregates (Fig. 1f, S4). We conclude that *ifc* is necessary for glial development and function in the larval nervous system.

To track the impact of *ifc* on glial morphology in the CNS, we paired GAL4 lines specific for each glial subtype with a UAS-linked membrane-tagged GFP transgene (Myr-GFP) and the MultiColor FlpOut technique (Kremer et al., 2017; Pfeiffer et al., 2010; Nern et al., 2015). Using this approach, we determined that loss of *ifc* function affects all CNS glial subtypes except perineurial glia (Fig. 2e-e', j-j'). Cortex glia appeared swollen, failed to enwrap neurons, and accumulated large amounts of Myr-GFP^{+} internal membranes (Fig. 2a-a', 2f-f'). Ensheathing glia (Fig. 2b-b', g-g') and subperineurial glia (Fig. d-d', i-l') also displayed swollen, disorganized cell bodies and accumulated Myr-GFP^{+} internal membranes. Astrocyte-like glia displayed smaller cell bodies, reduced membrane extensions, and disrupted organization along the dorsal ventral nerve cord (Fig. 2c-c'). We conclude that *ifc* regulates the morphology of most glial subtypes in the larval CNS.

Next, we asked if loss of *ifc* function alters the number of each glial subtype. Using the same glial subtype-specific GAL4 lines to drive a nuclear-localized GFP transgene, we counted the total number of all CNS glial subtypes, except perineurial glia, in wild type and *ifc*$^{-/-}$ larvae. To remove the small size of the brain in *ifc*$^{-/-}$ larvae as a confounding factor, we focused our analysis on the ventral nerve cord. The number of subperineurial glia was unchanged between the two genotypes, but we observed a 12%, 40%, and 72% reduction in the number of astrocyte-like,

ensheathing, and cortex glia, respectively, in *ifc*$^{-/-}$ larvae relative to wild-type (Fig. 2k-n). Our data demonstrate a broad role for *ifc* in regulating glial cell morphology and number in the *Drosophila* larval CNS.

***ifc* acts in glia to regulate glial and CNS development**

Prior work in zebrafish showed that *DEGS1* knockdown reduced the number of myelin basic protein-positive oligodendrocytes (Pant et al., 2019); in flies, loss of *ifc* function in the eye drove photoreceptor neuron degeneration (Jung et al., 2017). But neither study uncovered the cell type in which *ifc/DEGS1* acts to regulate neural development. To address this question, we used the GAL4/UAS system, RNAi-mediated gene depletion, and gene rescue approaches to see if *ifc* acts in neurons or glia to control glial development and CNS morphology. First, we used a UAS-linked *ifc*-RNAi transgene to deplete *ifc* function in all neurons (*elav-GAL4*; *repo-GAL80*) or all glia (*repo-GAL4*). Focusing on FABP-positive cortex glia due to their easily scorable phenotype, we found that pan-neuronal knockdown of *ifc* had no effect (Fig. 3c, j), but that pan-glial knockdown of *ifc* recapitulated the swollen cortex glia phenotype observed in *ifc* mutant larvae (Fig. 3d, j).

To complement our RNAi approach, we asked if GAL4-driven expression of a wild-type *Drosophila ifc* or human *DEGS1* transgene rescued the *ifc*$^{-/-}$ CNS mutant phenotype. In the absence of a GAL4 driver, the *ifc* transgene drove weak rescue of the cortex glia phenotype (Fig. 3e, k), consistent with modest GAL4-independent transgene expression reported for UAS-linked transgenes (Southall et al., 2013). Pan-neuronal expression of *ifc* drove modest rescue of the *ifc* CNS phenotype beyond that observed for the *ifc* transgene alone (Fig 3f, k), but pan-glial expression of *ifc* fully rescued the *ifc* mutant cortex glia phenotype and other CNS phenotypes (Figs. 3h, k and S3). Identical experiments using the human *DEGS1* transgene revealed that only pan-glial *DEGS1* expression provided rescuing activity (Fig. 3g, i, k). We infer that *ifc* acts primarily

in glia to govern CNS development and that human *DEGS1* can partially substitute for *ifc* function in flies despite a difference in the preferred length of the sphingoid backbone in flies (14 carbons) versus mammals (18 carbons) (Fyrst et al., 2004).

***ifc* is predominately expressed in glia and localizes to the ER**

Next, we used RNA in-situ hybridization and an *ifc-T2A-GAL4* transcriptional reporter to track *ifc* expression in the CNS. RNA in-situ hybridization revealed that *ifc* is widely expressed in the CNS (Fig. 4a), most obviously in the distinctive star-shaped astrocyte-like glia (Fig. 4b), which are marked by Ebony expression (Zeigler et al., 2013). RNA in-situ hybridization was not, however, ideal for tracing *ifc* expression in other cells, likely due to signal diffusion. To address this problem, we paired *ifc-T2A-GAL4* with a nuclear RFP (nRFP) transgene (He et al., 2019) and confirmed authenticity of the *ifc-T2A-GAL4* line by its strong expression in astrocyte-like glia (Fig. 4c). Using this approach, we found that *ifc* is strongly expressed in all glial cells (Fig. 4e-f) and weakly in most neurons in the larval CNS (Fig. 4d, g).

Using a fosmid transgene that harbors a GFP-tagged version of *ifc* flanked by ~36-kb of its endogenous genomic region as well as molecular markers for ER, cis-Golgi, and trans-Golgi (Sarov et al., 2016; Bergeron et al., 1994; Kikuma et al., 2017; Park et al., 2022), we found that the Ifc-GFP colocalized strongly with the ER markers Calnexin 99A (Cnx99A) and ESYT (Fig. 5a-b) and weakly with the cis-Golgi marker GOLGIN84 (Fig. 5c) and the trans-Golgi marker GOLGIN245 (Fig. 5d). Our results indicate that Ifc localizes primarily to the ER, aligning with the presumed site of de novo ceramide biosynthesis (Kawano et al., 2006) and prior work on *DEGS1* localization in human cell lines (Karsai et al., 2019).

Loss of *ifc* drives ER expansion and lipid droplet loss in cortex glia

Next, we asked if loss of *ifc* function altered ER, Golgi, or lysosome morphology. Focusing on cortex glia, we observed a clear expansion of the ER marker CNX99A (Fig. 5e-e'), a mild enrichment of the Golgi markers, Golgin-84 and Golgin-245, in diffuse "clouds" (Fig. 5f-f', g-g'), and a reduction in expression of the lysosome marker LAMP in *ifc*$^{-/-}$ larvae. The expansion of ER markers in *ifc* mutant larvae compelled us to obtain high-resolution views of organelle structure in cortex glia via transmission electron microscopy (TEM). In wild-type, cortex glia display a compact cytoplasm that surrounds a large nucleus (Fig. 6a-b) and extend glial sheaths that fully enwrap adjacent neuronal cell bodies (black arrows, Fig. 6c-d). In *ifc*$^{-/-}$ larvae, cortex glia display enlarged cell bodies with a maze-like pattern of internal membrane structures (solid white arrows, Fig. 6a'-b' & e-e') and fail enwrap neurons (hollow white arrows, Fig. 6c'-d'). The accumulated internal membrane structures appear to assume an ER-like identity, as we observed significant overlap between the ER marker Cnx99A and the membrane marker Myr-GFP when Myr-GFP was driven by a cortex glia-specific GAL4 line (Fig. 6f). We observed similar yet milder effects on cell swelling and internal membrane accumulation in subperineurial and wrapping glia in abdominal nerves (purple and pink shading, respectively, Fig. 6g-h), indicating that loss of *ifc* drives internal membrane accumulation in and swelling of multiple glial subtypes.

TEM analysis also revealed a near complete depletion of lipid droplets in the CNS of *ifc*$^{-/-}$ larvae (compare Fig. 6a, c-d to 6a', c'-d'; lipid droplets marked by asterisk; Fig. 6m), which we confirmed using BODIPY to mark neutral lipids in FABP-positive cortex glia (Fig. 6i-j & k-l). In the CNS, lipid droplets form primarily in cortex glia (Kis et al., 2015) and are thought to act as building blocks of membrane lipids versus an energy source in the brain (Grabner et al., 2021). Consistent with lipid droplet depletion indicating increased membrane lipid biogenesis, RNA-seq assays of dissected nerve cords revealed that loss of *ifc* drove transcriptional upregulation of genes that promote membrane lipid biogenesis, such as *SREBP*, the conserved master regulator of lipid

biosynthesis, *SCAP*, an activator of SREBP, and *Pcyt1/Pcyt2,* which promote phosphatidylcholine and phosphatidylethanolamine synthesis (Fig. 6j; Eberlé et al., 2004; Osborne & Espenshad, 2009; Jacquemyn et al., 2017). The spliced form of *Xbp-1* mRNA (*Xbp-1s*) (Fig. 6j), which promotes membrane lipid synthesis required for ER biogenesis and is activated by the unfolded protein response (UPR) (Sriburi et al., 2007), is also upregulated in the CNS of *ifc* mutant larvae. Most ER chaperones, which are typically transcriptionally upregulated upon UPR activation (Bernales et al., 2006), were however downregulated (Fig. S5), suggesting that in this case loss of *ifc* triggers increased membrane biogenesis but not UPR activation. Similar results have been observed in yeast, where ER expansion has been shown to alleviate ER stress independently of the unfolded protein response (Schuck et al., 2009)

Loss of *ifc* increases the saturation levels of triacylglycerols and membrane phospholipids

Lipid droplets are composed largely of triacylglycerols (TGs) (Jacquemyn et al., 2017), and we observed a 5-fold and 3-fold drop in TG levels in the CNS and whole larvae of *ifc* mutant larvae relative to wild-type (Fig. 7a). Our metabolomic analysis also revealed a shift of TGs toward higher saturation levels in the absence of *ifc* function (Fig. 7a-c). In support of this idea, we observed transcriptional upregulation of most genes in the Lands cycle, which remodels phospholipids by replacing existing fatty acyl groups with new fatty acyl groups (Fig. S9) (Moessinger et al., 2011; Moessinger et al., 2014; Harayama et al., 2014; O'Donnell, 2022). As TGs function as building blocks of membrane phospholipids, we asked if changes in TG levels and saturation were reflected in the levels or saturation of the membrane phospholipids phosphatidylcholine (PC), phosphatidylethanolamine (PE), and phosphatidylserine (PS). In the absence of *ifc* function, PC and PE exhibited little change in quantity (Fig. 7d & g), but the less abundant PS exhibited a roughly three-fold increase in quantity in the CNS of *ifc* mutant larvae relative to wild-type (compare Fig. 7j to Fig. 7d & g). All three phospholipids, however, displayed

increased saturation levels: The relative levels of all PC, PE, and PS species were reduced, except for the most saturated form of each phospholipid – 18:1/18:1 – which is increased (Fig. 7e-f, h-i, & k-l). This increase was more pronounced in the CNS than whole larvae (Fig. 7f, i, & l), implying that loss of *ifc* function creates greater demand for lipid remodeling in the CNS. We speculate that increased PC, PE, and PS saturation in *ifc* mutants is a compensatory mechanism that seeks to stabilize the more rigid cell membranes caused by increased presence of dihydroceramide species.

Reduction of dihydroceramide synthesis suppresses the *ifc* CNS phenotype

Following its synthesis, CERT transports ceramide from the ER to the Golgi, but CERT is less efficient at transporting dihydroceramide than ceramide (REF). The expanded nature of the ER in *ifc* mutant larvae supports a model in which loss of *ifc* triggers the accumulation and inappropriate retention of dihydroceramide in the ER, which drives ER expansion and glial swelling. If this model is correct, reduction of dihydroceramide levels should suppress the *ifc* CNS phenotype. In agreement with this model, we found that the *schlank*^{G0365} loss of function allele dominantly suppressed the *ifc* CNS elongation and enhanced RFP expression phenotypes (Fig. 8a-b). Second, we found that glial-specific depletion of *schlank* suppressed the CNS elongation, enhanced RFP expression, glial swelling, internal membrane accumulation, and lipid droplet depletion phenotypes observed in otherwise *ifc* mutant larvae (Fig. 8a-h). Our data support the model that inappropriate retention of dihydroceramide in the ER drives ER expansion and in turn glial swelling and dysfunction.

DISCUSSION

Our work on *ifc* supports a model in which loss of *ifc/DEGS1* function drives glial dysfunction through the accumulation and inappropriate retention of dihydroceramide in the ER with this proximal defect leading to ER expansion, cell swelling, and eventually neurodegeneration. A large increase in dihydroceramide would also impact ER membrane structure: ER membranes are typically loosely packed, thin, semi-fluid structures, with sphingolipids comprising just 3% of ER phospholipids (Jacquemyn et al., 2017). Sphingolipids in general and dihydroceramide in specific are highly saturated lipids, promote lipid order, tighter lipid packing, membrane rigidity, and thicker membranes (O'Brien, 1965; Marcus & Popko, 2002). Our observation of thick ER membranes in cortex glia in *ifc*$^{-/-}$ larvae (Fig. 6) aligns with increased dihydroceramide levels in the ER. In this context, we note that of many clinical observations made on an HLD-18 patient, one was widening of the ER in Schwann cells (Karsai et al., 2019), a finding that when combined with our work suggests that dihydroceramide accumulation in the ER is the proximal cause of HLD-18.

Although we think ER expansion represents the most proximal effect of loss of *ifc/DEGS1* function and dihydroceramide accumulation on cortex glia, other organelles and their functions are likely also disrupted, minimally as a secondary consequence of ER disruption. For example, the apparent reduction of the lysosome marker, LAMP1, in cortex glia of *ifc* mutant larvae correlates with increased RFP levels and the presence of bright RFP puncta or aggregates in this cell type, suggesting impaired lysosome function contributes to increased RFP perdurance and aggregation. Defects in the activity of multiple organelles may collaborate to elicit the full phenotype manifested by loss of *ifc/DEGS1* function, in the end resulting in nervous system dysfunction and neuronal degeneration.

Increased dihydroceramide levels may contribute to a broader spectrum of neurodegenerative diseases than simply HLD-18. Recent work reveals that gain of function mutations in *SPTLC1* and *SPTLC2*, which encode components of the SPT complex that catalyzes the initial, rate limiting step of de novo ceramide and sphingolipid biosynthesis (Harrison et al.,

2018), cause juvenile ALS via increased sphingolipid biosynthesis (Lone et al., 2022; Lone et al., 2023; Syeda et al., 2023; Dohrn et al., 2023). Of note, of all sphingolipids, the relative levels of dihydroceramide were increased the most in patient plasma samples, suggesting that DEGS1 activity becomes limiting in the presence of enhanced SPT activity and that dihydroceramide accumulation contributes to juvenile ALS. Any mutations that increase metabolite flux through the ceramide pathway upstream of DEGS1 may then increase dihydroceramide levels, drive ER expansion and cell swelling, and lead to neurodegeneration, with disease severity predicated on the extent of dihydroceramide accumulation. Model systems, like flies, may be able to harness the power of genetic modifier screens to identify genes and pathways, and thus potential therapeutic targets, that can be tweaked to ameliorate the effect of elevated dihydroceramide levels on neurodegeneration.

Our work appears to pinpoint the cell type impacted by loss of *ifc/DEGS1* function: Glia, specifically glia that exhibit great demand for membrane biogenesis like cortex glia in the fly and oligodendrocytes or Schwann cells during mammalian development. During larval development, *ifc* is expressed at higher levels in glial cells than in neurons, and its genetic function is required at a greater level in glia than neurons to govern CNS development. Our unpublished work on other genes in the ceramide metabolic pathway reveals similar glial-centric expression patterns in the larval CNS to that observed for *ifc*, suggesting they too function primarily in glia rather than neurons to control nervous system function during this stage. In support of this idea, a study on CPES, which converts ceramide into CPE, the fly analog of sphingomyelin, revealed that CPES is required in cortex glia to promote their morphology and homeostasis and to protect flies from photosensitive epilepsy (Kunduri et al., 2018)**.** Similarly, in mice ORMDL, a dedicated negative regulator of the SPT complex, is required in oligodendrocytes to maintain proper myelination (Clarke et al., 2019). Given that many glial cell types, including oligodendrocytes in the mammalian system, are enriched in sphingolipids and exhibit a great demand for new membrane

biogenesis during phases of rapid neurogenesis and axonogenesis, we speculate that glial cells, such as cortex glia, oligodendrocytes, and Schwann cells, rather than neurons manifest a greater need for *ifc/DEGS1* function and ceramide synthesis during developmental stages marked by significant nervous system growth.

Will this glial-centric model for *ifc/DEGS1* function, and more generally ceramide synthesis, hold true in the adult when neurogenesis is largely complete and the demand for new membrane synthesis in glia dissipates? Recent work in the adult fly eye suggests it may not. Wang et al. (2022) showed that the GlcT enzyme, which converts ceramide to glucosylceramide, is expressed at much higher levels in neurons than glia, and that glucosylceramide is then transported from neurons to glial cells for its degradation, suggesting cell-type specific compartmentalization of sphingolipid synthesis in neurons and its degradation in glia in the adult. In the future, it will be exciting to follow whether genes of the sphingolipid metabolic pathway act primarily in glia or neurons to regulate nervous system development and function, and whether any cell-type specific requirement for a gene switches as a function of developmental stage.

Altered glial function may derive not just from dihydroceramide buildup in the ER, but also from altered cell membrane structure due to the replacement of ceramide and its derivates, such as GlcCer and CPE, with the cognate forms of dihydroceramide. Relative to dihydroceramide species, the 4-5 *trans* carbon double bond in the sphingoid backbone of ceramide-containing sphingolipids enables them to form more stable hydrogen bonds with water molecules and facilitates their ability to associate with lipids of different saturation levels (Li et al., 2002; Gilliams et al., 2015). High levels of dihydroceramide or a high dihydroceramide to ceramide ratio has been shown to form rigid gel-like domains within model membranes and to destabilize biological membranes by promoting their permeabilization (Viera et al., 2010; Hernández-Tiedra et al., 2016). As even minor alterations to membrane properties can disrupt glial morphology (Aggarwal, Yurlova, & Simons, 2011), such alterations in membrane rigidity and stability may underlie the

failure of cortex glia to enwrap adjacent neurons. The observed increase in saturation of PE, PC, and PS in the CNS of *ifc* mutant larvae may reflect a compensatory response employed by cells to stabilize cell membranes when challenged with elevated levels of dihydroceramide.

The observed loss of lipid droplets in cortex glia may also contribute to their inability to fully enwrap neuronal cell bodies. Under wild-type conditions, many lipid droplets are present in cortex glia during the rapid phase of neurogenesis that occurs in larvae. During this phase, lipid droplets likely support the ability of cortex glia to generate large quantities of membrane lipids to drive membrane growth needed to ensheath newly born neurons. Supporting this idea, lipid droplets disappear in the adult *Drosophila* CNS when neurogenesis is complete and cortex glia remodeling stops (Kis et al., 2015). We speculate that lipid droplet loss in *ifc* mutant larvae contributes to the inability of cortex glia to enwrap neuronal cell bodies. Prior work on lipid droplets in flies has focused on stress-induced lipid droplets generated in glia and their protective or deleterious roles in the nervous system (Bailey et al., 2015; Liu et al., 2015; Liu et al., 2017). Work in mice and humans has found that more lipid droplets are often associated with the pathogenesis of neurodegenerative diseases (Marshall et al., 2014; Farmer et al., 2020; Marschallinger et al., 2020), but our work correlates lipid droplet loss with CNS defects. In the future, it will be important to determine how lipid droplets impact nervous system development and disease.

Acknowledgements

We thank the Iowa Developmental Studies Hybridoma Bank for antibodies, and the Bloomington Stock Center, Vienna Drosophila Research Center, FlyORF, and the National Institutes of Genetics stock center in Japan for countless fly lines. We thank Dr. Christian Klambt and Dr. Chih-Chiang Chan for fly lines, and Dr. Dion Dickman for the ESYT antibody. We thank Dr. Tristan Li for comments on the manuscript. We thank the Genome Technology Access Center (GTAC) at Washington University for next-generation sequencing and analysis of the RNA-seq samples. We

gratefully acknowledge Dr. Sanja Sviben, Gregory Strout, and John Wullf II for assistance in electron microscopy studies conducted at the Washington University Center for Cellular Imaging (WUCCI), which is supported in part by Washington University School of Medicine, The Children's Discovery Institute of Washington University and St. Louis Children's Hospital (CDI-CORE-2015-505 and CDI-CORE-2019-813), the Foundation for Barnes-Jewish Hospital (3770) and the Washington University Diabetes Research Center (NIH P30 DK020579).

Author Contributions

BAW, HL, Yi Zhu, and JBS completed the genetic screen that identified the *ifc* alleles and completed the initial genetic characterization of these alleles. Yuqing Zhu, JD, and JBS completed all other experiments except for the metabolomic analyses, which were completed by KC and GJP. Yuqing Zhu and JBS wrote the manuscript and compiled figures with help from JD with figures. All authors read, commented on, and edited the manuscript.

Funding: This work was supported by grants from the National Institutes of Health (NS036570) to J.B.S., (NS122903) to H.L., and (R35 ES2028365) to G.J.P.

Competing interests: G.J.P. is a scientific advisory board member for Cambridge Isotope Laboratories and has collaborative research agreements with Bruker Corporation and Thermo Scientific. G.J.P. is the chief scientific officer of Panome Bio. The remaining authors declare no competing interests.

Methods

Fly husbandry: Flies were raised on standard molasses-based food at 25°C. Unless otherwise noted, wild type is an otherwise wild-type stock harboring the *M{3xP3-RFP.attP}ZH-51D* insert in an isogenic second chromosome.

Mutagenesis: A standard autosomal recessive forward genetic screen was carried out using 25-30 µm EMS to mutagenize a *M{3xP3-RFP.attP}ZH-51D* isogenic second chromosome. Homozygous mutant third instar larvae were visually screened under a standard fluorescent microscope for defects in CNS morphology. A detailed description of the screen and all other identified genes will be described elsewhere.

Creation of recombinant lines and identification of second site mutations in *ifc-KO* chromsome

Standard genetic methods were used to generate fly strains that contained specific combinations of GAL4 and UAS-linked transgenes in the ifc^{js3} or *ifc-KO* background. During this process, we uncovered that the *ifc-KO* deletion could be unlinked from at least one second chromosomal mutation that caused early larval lethality, resulting in homozygous *ifc-KO* flies that survived to late L3 to early pupa. A subsequent EMS-based F2 lethal non-complementation screen using the *M{3xP3-RFP.attP}ZH-51D* isogenic second chromosome as target chromosome and screening against the *ifc-KO* chromosome identified multiple mutations in four complementation groups that led to an early larval lethal phenotype. Whole genome sequencing identified these genes as *Med15*, *lwr*, *Nle*, and *Sf3b1*; all four genes reside within ~90 Kb of each other in chromosomal bands 21D1-21E2 near the telomere in chromosome 2L, identifying the site of the associated lethal mutations and suggesting the actual lesion may be a small deletion that removes these genes. The following alleles of these genes are available at Bloomington Stock Center: $Med15^{js1}$

(Q175*), *Med15*^{js2} (Q398*), *Med15*^{js3} (C655Y), *lwr*^{js1} (I4N), *lwr*^{js2}(E12K), *Nle*^{js1} (W146R), *Nle*^{js2} (L125P), *Nle*^{js3} (Q242*), *Sf3b1*^{js1} (R1160*), *Sf3b1*^{js2} (Q1264*), *Sf3b1*^{js3} (570 bp deletion at the following coordinates chr2L571720-572290; this deletion removes amino acids 1031 through 1222 and introduces a frameshift into the reading frame).

Gene rescue and in vivo RNAi phenocopy assays

To restrict UAS-linked transgene expression specifically to glia, we used the *repoGAL4* driver line. To restrict UAS-linked transgene expression specifically to neurons, we paired the *elavGAL4* driver lines, which activates transgene expression strongly in all neurons and moderately in glia, with *repoGAL80*, which blocks GAL4-dependent activation in glia. We used *P{VSH330794}* (VDRC 330794) for the RNAi experiments and *UAS-ifc* (Bischof et al., 2013) and *UAS-DEGS1* (BDSC 79200) for the gene rescue assays. All gene rescue experiments were performed in the *ifc*^{js3}/*ifc-KO* background with the UAS-transgene placed into the *ifc*^{js3} background and the GAL4 drivers into the *ifc-KO* background.

The GAL4-UAS method was also used to assess the phenotype of each glial subtype. In combination with the *UAS-Myr-GFP* transgene, which labels cell membranes, we used the following GAL4 lines to trace the morphology of each glial subtype in wild type and *ifc*$^{-/-}$ larvae: *GMR85G01-GAL4* (perineurial glia; BDSC 40436), *GMR54C07-GAL4* (subperineurial glia; BDSC 50472), *GMR54H02-GAL4* (cortex glia; BDSC 45784), *GMR56F03-GAL4* (ensheathing glia; BDSC 77469 and 39157), and *GMR86E01-GAL4* (astrocyte-like glia; BDSC45914). The *UAS-Myr-GFP* transgene was placed into the *ifc*^{js3} background; each glial GAL4 line was placed into the *ifc-KO* background.

DNA sequencing: Genomic DNA was obtained from wild type larvae or larvae homozygous for each relevant mutant line and provided to GTAC (Washington University) or GENEWIZ for next-generation or Sanger sequencing.

RNA in-situ hybridization: *ifc* RNA probes for in-situ hybridization chain reaction (HCR) were designed and made by Molecular Instruments (HCR™ RNA-FISH v3.0; Choi et al. 2018). Wild type CNS was harvested and fixed in 2% paraformaldehyde at late L3. The fixed CNS underwent gradual dehydration and rehydration, followed by standard hybridization and amplification steps of the HCR protocol (Choi et al. 2018). For double labeling with antibody, the post-HCR labeled CNS was briefly fixed for 30 minutes prior to standard antibody labeling protocol to identify specific CNS cell type(s) with highly localized *ifc* RNAs (Lacin et al., 2019; Duckhorn et al., 2022).

MultiColor FlpOut labeling of glial subtypes

For glial labeling in the control background, the *MCFO1* line was crossed to *GMR-GAL4* driver lines for each glial subtype (Supplemental Table 1; Nern et al. 2015). For glial labeling in $ifc^{-/-}$ background, the *MCFO1* line was placed in the ifc^{JS3} background, each of the five glial-specific GMR-GAL4 lines were placed individually into the *ifc-KO* background, and then the MCFO, ifc^{JS3} line was crossed to each glial specific GAL4, *ifc-KO* line. Flies were allowed to lay eggs for 24 hr at 25°C, and progeny were raised at 25°C for 4 days prior to heat-activated labeling. On day 4 after egg-laying, F1 larvae were incubated in a 37°C water bath for 5-minutes. When wild-type or $ifc^{-/-}$ mutant larvae reached late L3, which was day 5-6 for control and day 9-10 for $ifc^{-/-}$ mutants, the CNS was dissected, fixed, stained, and then analyzed under a Zeiss LSM 700 Confocal Microscope for the presence of clones, using Zen software.

Antibody generation: YenZym (CA, USA) was used as a commercial source to generate affinity purified antibodies against a synthetic peptide that corresponded to amino acids 85-100 (TLDGNKLTQEQKGDKP) of FABP isoform B. Briefly, the peptide was conjugated to KLH, used as an immunogen in rabbits to generate a peptide-specific antibody response, and antibodies specific to the peptide were affinity purified. The affinity-purified antibodies were confirmed to label cortex glia specifically based on comparison of antibody staining relative to Myr-GFP when a UAS-Myr-GFP was driven under control of the cortex specific glial GAL4 driver GMR-54H02 (Fig. S-pending). The FABP antibodies are used at 1:500-1:1000.

Immunofluorescence and lipid droplet staining: Gene expression analysis was performed essentially as described in Patel (1994). Briefly, the larval CNS was dissected in PBS, fixed in 2.5% paraformaldehyde for 55 minutes, and washed in PTx (1xPBS, 0.1% TritonX-100. The fixed CNS was incubated in primary antibody with gentle rocking overnight at 4°C. Secondary antibody staining was conducted for at least two hours to overnight at room temperature. All samples were washed in PTx at least five times and rocked for an hour before and after secondary antibody staining. A detailed list of the primary and secondary antibodies is available in Supplemental Table 2. Dissected CNS were mounted either in PTx or dehydrated through an ethanol series and cleared in xylenes prior to mounting in DPX mountant (Truman et al., 2004). All imaging was performed on a Zeiss LSM-700 Confocal Microscope, using Zen software.

For lipid droplet staining, the fixed CNS was incubated for 30 minutes at room temperature at 1:200 dilution of 1mg/mL BODIPY™ 493/503 (Thermo Fisher Scientific: D3922). It was then rinsed thoroughly in PBS and immediately mounted for imaging on a Zeiss LSM-700 Confocal Microscope, using Zen software.

Transmission electron microscopy (TEM) imaging

For transmission electron microscopy (TEM), samples were immersion fixed overnight at 4°C in a solution containing 2% paraformaldehyde and 2.5% glutaraldehyde in 0.15 M cacodylate buffer with 2 mM CaCl2, pH 7.4. Samples were then rinsed in cacodylate buffer 3 times for 10 minutes each and subjected to a secondary fixation for one hour in 2% osmium tetroxide/1.5% potassium ferrocyanide in cacodylate buffer. Following this, samples were rinsed in ultrapure water 3 times for 10 minutes each and stained overnight in an aqueous solution of 1% uranyl acetate at 4˚C. After staining was complete, samples were washed in ultrapure water 3 times for 10 minutes each, dehydrated in a graded acetone series (50%, 70%, 90%, 100% x4) for 15 minutes in each step, and infiltrated with microwave assistance (Pelco BioWave Pro, Redding, CA) into Spurr's resin. Samples were then cured in an oven at 60˚C for 72 hours and post-curing, 70 nm thin sections were cut from the resin block, post-stained with uranyl acetate and Sato's lead and imaged on a Transmission Electron Microscope (JEOL JEM-1400 Plus, Tokyo, Japan) operating at 120 KeV.

Metabolomics

Untargeted lipidomics analysis was conducted on whole larva and dissected CNS of wild type and *ifc*$^{-/-}$ mutants at the late-third instar stage. Five replicates were prepared for each set of experiments. For whole larvae, at least 15 larvae of each genotype were used for each replicate. For the dissected CNS, at least 50 wild type and 60 *ifc*$^{-/-}$ CNS were used per replicate. Immediately following collection or dissection, larvae and the dissected CNS were flash frozen in liquid nitrogen and placed at -80°C.

Lipids were extracted from frozen whole larvae and dissected larval CNS samples by using an Omni Bead Ruptor Elite Homogenizer using acetonitrile:methanol:water (2:2:1; 40 μL/mg tissue).

Two Ultrahigh performance LC-(UHPLC)/MS systems were used in this work: a Thermo Vanquish Flex UHPLC system with a Thermo Scientific Orbitrap ID-X and an Agilent 1290 Infinity II UPLC system with an Agilent 6545 QTOF as described previously (Cho et al., 2019). Lipids were separated on a Waters Acquity HSS T3 column (150 x 2.1 mm, 1.8 mm). The mobile-phase solvents were composed of A: 0.1% formic acid, 10 mM ammonium formate, 2.5 mM medronic acid in 60:40 acetonitrile:water; and B = 0.1% formic acid, 10 mM ammonium formate in 90:10 2-propanol:acetonitrile. The column compartment was maintained at 60 °C. The following linear gradient was applied at a flow rate of 0.25 mL min-1: 0 – 2 min, 30% B; 17 min, 75% B; 20 min, 85% B; 23 – 26 min, 100% B. The injection volume 4 mL for all lipids analysis. Data was acquired in positive ion.

LC/MS data were processed and analyzed with the open-source Skyline software (Adams et al., 2020). Lipid MS/MS data were annotated with Agilent Lipid Annotator software.

RNA sequencing and analysis

To determine the CNS-specific transcriptional changes upon loss of *ifc*, RNA-seq was conducted on five replicates of dissected CNS tissue derived from wild type and *ifc*$^{-/-}$ mutant late-third instar larvae. For each replicate, roughly 30-35 dissected CNS of wild type or *ifc-/-* larvae were used. Invitrogen™ RNAqueous™-Micro Total RNA Isolation Kit (AM1931) was used to extract RNA. Agilent 4200 TapeStation system was used for RNA quality control.

Samples were prepared according to library kit manufacturer's protocol, indexed, pooled, and sequenced on an Illumina NovoSeq. Basecalls and demultiplexing were performed with Illumina's bcl2fastq software and a custom python demultiplexing program with a maximum of one mismatch in the indexing read. RNA-seq reads were then aligned to the Ensembl release 76 primary assembly with STAR version 2.5.1a (Dobin et al., 2013). Gene counts were derived from

the number of uniquely aligned unambiguous reads by Subread:featureCount version 1.4.6-p5 (Liao et al., 2014). Isoform expression of known Ensembl transcripts were estimated with Salmon version 0.8.2 (Patro et al., 2017). To find the most critical genes, the raw counts were variance stabilized with the R/Bioconductor package DESeq2 (Love et al., 2014) and was then analyzed via weighted gene correlation network analysis with the R/Bioconductor package WGCNA (Langfelder and Horvath, 2018).

Statistics: All data are presented as mean ± SEM. Statistical significance between groups was determined using Student's *t*-test or one-way ANOVA with multiple comparisons, and with varying levels of significance assessed as * $P < 0.05$, ** $P < 0.01$, *** $P < 0.001$, **** $P < 0.0001$, and ns, not significant.

REFERENCES

Acharya, U., & Acharya, J. K. (2005). Enzymes of sphingolipid metabolism in *Drosophila melanogaster*. *Cellular and Molecular Life Sciences CMLS*, *62*, 128-142.

Adams, K. J., Pratt, B., Bose, N., Dubois, L. G., St. John-Williams, L., Perrott, K. M., ... & Alzheimer's Disease Metabolomics Consortium. (2020). Skyline for small molecules: a unifying software package for quantitative metabolomics. *Journal of proteome research*, *19*(4), 1447-1458.

Aggarwal, S., Yurlova, L., & Simons, M. (2011). Central nervous system myelin: structure, synthesis and assembly. *Trends in cell biology*, *21*(10), 585-593.

Bailey, A. P., Koster, G., Guillermier, C., Hirst, E. M., MacRae, J. I., Lechene, C. P., ... & Gould, A. P. (2015). Antioxidant role for lipid droplets in a stem cell niche of Drosophila. *Cell*, *163*(2), 340-353.

Bejaoui, K., Wu, C., Scheffler, M. D., Haan, G., Ashby, P., Wu, L., ... & Brown, R. H. (2001). SPTLC1 is mutated in hereditary sensory neuropathy, type 1. *Nature genetics*, *27*(3), 261-262.

Bergeron, J. J., Brenner, M. B., Thomas, D. Y., & Williams, D. B. (1994). Calnexin: a membrane-bound chaperone of the endoplasmic reticulum. *Trends in biochemical sciences*, *19*(3), 124-128.

Bernales, S., Papa, F. R., & Walter, P. (2006). Intracellular signaling by the unfolded protein response. *Annu. Rev. Cell Dev. Biol.*, *22*, 487-508.

Bischof, J., Björklund, M., Furger, E., Schertel, C., Taipale, J., & Basler, K. (2013). A versatile platform for creating a comprehensive UAS-ORFeome library in *Drosophila*. *Development*, *140*(11), 2434-2442.

Blackburn, N. B., Michael, L. F., Meikle, P. J., Peralta, J. M., Mosior, M., McAhren, S., ... & Curran, J. E. (2019). Rare DEGS1 variant significantly alters de novo ceramide synthesis pathway [S]. *Journal of lipid research*, *60*(9), 1630-1639.

Bolaños, J. P., Heales, S. J., Land, J. M., & Clark, J. B. (1995). Effect of peroxynitrite on the mitochondrial respiratory chain: differential susceptibility of neurones and astrocytes in primary culture. *Journal of neurochemistry*, *64*(5), 1965-1972.

Borrego, S. L., Fahrmann, J., Hou, J., Lin, D. W., Tromberg, B. J., Fiehn, O., & Kaiser, P. (2021). Lipid remodeling in response to methionine stress in MDA-MBA-468 triple-negative breast cancer cells. *Journal of lipid research*, *62*.

Chaudhry, N., Sica, M., Surabhi, S., Hernandez, D. S., Mesquita, A., Selimovic, A., ... & Jenny, A. (2022). Lamp1 mediates lipid transport, but is dispensable for autophagy in *Drosophila*. *Autophagy*, *18*(10), 2443-2458.

Chintapalli, V. R., Wang, J., & Dow, J. A. (2007). Using FlyAtlas to identify better *Drosophila melanogaster* models of human disease. *Nature genetics*, *39*(6), 715-720.

Cho, K., Schwaiger-Haber, M., Naser, F. J., Stancliffe, E., Sindelar, M., & Patti, G. J. (2021). Targeting unique biological signals on the fly to improve MS/MS coverage and identification efficiency in metabolomics. *Analytica chimica acta*, *1149*, 338210.

Choi, H. M., Schwarzkopf, M., Fornace, M. E., Acharya, A., Artavanis, G., Stegmaier, J., Cunha, A., & Pierce, N. A. (2018). Third-generation in situ hybridization chain reaction: multiplexed, quantitative, sensitive, versatile, robust. *Development*, *145*(12), dev165753.

Clarke BA, Majumder S, Zhu H, Lee YT, Kono M, Li C, Khanna C, Blain H, Schwartz R, Huso VL, Byrnes C, Tuymetova G, Dunn TM, Allende ML, Proia RL. (2019) The *Ormdl* genes regulate the sphingolipid synthesis pathway to ensure proper myelination and neurologic function in mice. Elife, *27* (8):e51067.

Coetzee, T., Fujita, N., Dupree, J., Shi, R., Blight, A., Suzuki, K., ... & Popko, B. (1996). Myelination in the absence of galactocerebroside and sulfatide: normal structure with abnormal function and regional instability. *Cell*, *86*(2), 209-219.

Corty, M. M., & Coutinho-Budd, J. (2023). Drosophila glia take shape to sculpt the nervous system. *Current Opinion in Neurobiology*, *79*, 102689.

Coutinho-Budd J, Freeman MR. (2013) Probing the enigma: unraveling glial cell biology in invertebrates. Current Opinion in Neurobiology. 23(6):1073-9.

Couttas, T. A., Kain, N., Suchowerska, A. K., Quek, L. E., Turner, N., Fath, T., ... & Don, A. S. (2016). Loss of ceramide synthase 2 activity, necessary for myelin biosynthesis, precedes tau pathology in the cortical pathogenesis of Alzheimer's disease. *Neurobiology of aging*, *43*, 89-100.

Dobin, A., Davis, C. A., Schlesinger, F., Drenkow, J., Zaleski, C., Jha, S., Batut, P., Chaisson, M., & Gingeras, T. R. (2013). STAR: ultrafast universal RNA-seq aligner. *Bioinformatics*, *29*(1), 15-21.

Dohrn, M. F., Beijer, D., Lone, M. A., Bayraktar, E., Oflazer, P., Orbach, R., ... & Zuchner, S. (2023). Recurrent de-novo gain-of-function mutation in SPTLC2 confirms dysregulated sphingolipid production to cause juvenile amyotrophic lateral sclerosis. *Journal of Neurology, Neurosurgery & Psychiatry*.

Dolgin, V., Straussberg, R., Xu, R., Mileva, I., Yogev, Y., Khoury, R., Konen, O., Barhum, Y., Zvulunov, A., Mao, C. & Birk, O. S. (2019). *DEGS1* variant causes neurological disorder. *European Journal of Human Genetics*, *27*(11), 1668-1676.

Duckhorn, J. C., Junker, I. P., Ding, Y., & Shirangi, T. R. (2022). Combined in situ hybridization chain reaction and immunostaining to visualize gene expression in whole-mount *Drosophila* central nervous systems. In *Behavioral Neurogenetics* (pp. 1-14). New York, NY: Springer US.

Dunn, T. M., Tifft, C. J., & Proia, R. L. (2019). A perilous path: the inborn errors of sphingolipid metabolism. *Journal of lipid research*, *60*(3), 475-483.

Eberlé, D., Hegarty, B., Bossard, P., Ferré, P., & Foufelle, F. (2004). SREBP transcription factors: master regulators of lipid homeostasis. *Biochimie*, *86*(11), 839-848.

Ehlert, K., Frosch, M., Fehse, N., Zander, A., Roth, J., & Vormoor, J. (2007). Farber disease: clinical presentation, pathogenesis and a new approach to treatment. *Pediatric Rheumatology*, *5*(1), 1-7.

Eskelinen, E. L. (2006). Roles of LAMP-1 and LAMP-2 in lysosome biogenesis and autophagy. *Molecular aspects of medicine*, *27*(5-6), 495-502.

Farmer, B. C., Walsh, A. E., Kluemper, J. C., & Johnson, L. A. (2020). Lipid droplets in neurodegenerative disorders. *Frontiers in neuroscience*, *14*, 742.

Freeman, M. R., & Doherty, J. (2006). Glial cell biology in Drosophila and vertebrates. *Trends in neurosciences*, *29*(2), 82-90.

Freeman, M. R. (2015). *Drosophila* central nervous system glia. *Cold Spring Harbor perspectives in biology*, *7*(11), a020552.

Fyrst, H., Herr, D. R., Harris, G. L., & Saba, J. D. (2004). Characterization of free endogenous C14 and C16 sphingoid bases from *Drosophila melanogaster*. *Journal of lipid research*, *45*(1), 54-62.

Gillams, R. J., Busto, J. V., Busch, S., Goñi, F. M., Lorenz, C. D., & McLain, S. E. (2015). Solvation and hydration of the ceramide headgroup in a non-polar solution. *The Journal of Physical Chemistry B*, *119*(1), 128-139.

Grabner, G. F., Xie, H., Schweiger, M., & Zechner, R. (2021). Lipolysis: cellular mechanisms for lipid mobilization from fat stores. *Nature metabolism*, *3*(11), 1445-1465.

Ghosh, A., Kling, T., Snaidero, N., Sampaio, J. L., Shevchenko, A., Gras, H., ... & Simons, M. (2013). A global in vivo *Drosophila* RNAi screen identifies a key role of ceramide phosphoethanolamine for glial ensheathment of axons. *PLoS genetics*, *9*(12), e1003980.

Hagen, R. M., Rodriguez-Cuenca, S., & Vidal-Puig, A. (2010). An allostatic control of membrane lipid composition by SREBP1. *FEBS letters*, *584*(12), 2689-2698.

Hannun, Y. A., & Obeid, L. M. (2018). Sphingolipids and their metabolism in physiology and disease. *Nature reviews Molecular cell biology*, *19*(3), 175-191.

Harayama, T., Eto, M., Shindou, H., Kita, Y., Otsubo, E., Hishikawa, D., ... & Shimizu, T. (2014). Lysophospholipid acyltransferases mediate phosphatidylcholine diversification to achieve the physical properties required in vivo. *Cell metabolism*, *20*(2), 295-305.

Harrison, P. J., Dunn, T. M., & Campopiano, D. J. (2018). Sphingolipid biosynthesis in man and microbes. *Natural product reports*, *35*(9), 921-954.

Harty, B. L., & Monk, K. R. (2017). Unwrapping the unappreciated: recent progress in Remak Schwann cell biology. *Current Opinion in Neurobiology*, *47*, 131-137.

He, L., Binari, R., Huang, J., Falo-Sanjuan, J., & Perrimon, N. (2019). In vivo study of gene expression with an enhanced dual-color fluorescent transcriptional timer. *Elife*, *8*, e46181.

Hernández-Tiedra, S., Fabrias, G., Dávila, D., Salanueva, I. J., Casas, J., Montes, L. R., ... & Velasco, G. (2016). Dihydroceramide accumulation mediates cytotoxic autophagy of cancer cells via autolysosome destabilization. *Autophagy*, *12*(11), 2213-2229.

Herrero-Mendez, A., Almeida, A., Fernández, E., Maestre, C., Moncada, S., & Bolaños, J. P. (2009). The bioenergetic and antioxidant status of neurons is controlled by continuous degradation of a key glycolytic enzyme by APC/C–Cdh1. *Nature cell biology*, *11*(6), 747-752.

Holland, W. L., Brozinick, J. T., Wang, L. P., Hawkins, E. D., Sargent, K. M., Liu, Y., ... & Summers, S. A. (2007). Inhibition of ceramide synthesis ameliorates glucocorticoid-, saturated-fat-, and obesity-induced insulin resistance. *Cell metabolism*, *5*(3), 167-179.

Jackman N, Ishii A, Bansal R. (2009) Oligodendrocyte development and myelin biogenesis: parsing out the roles of glycosphingolipids. Physiology, 24:290-7.

Jacquemyn, J., Cascalho, A., & Goodchild, R. E. (2017). The ins and outs of endoplasmic reticulum-controlled lipid biosynthesis. *EMBO reports*, *18*(11), 1905-1921.

Jung, W. H., Liu, C. C., Yu, Y. L., Chang, Y. C., Lien, W. Y., Chao, H. C., Huang, S.Y., Kuo, C.H., Ho, H.C., & Chan, C. C. (2017). Lipophagy prevents activity-dependent neurodegeneration due to dihydroceramide accumulation *in vivo*. *EMBO reports*, *18*(7), 1150-1165.

Karsai, G., Kraft, F., Haag, N., Korenke, G. C., Hänisch, B., Othman, A., ... & Kurth, I. (2019). DEGS1-associated aberrant sphingolipid metabolism impairs nervous system function in humans. *The Journal of clinical investigation*, *129*(3), 1229-1239.

Kasischke, K. A., Vishwasrao, H. D., Fisher, P. J., Zipfel, W. R., & Webb, W. W. (2004). Neural activity triggers neuronal oxidative metabolism followed by astrocytic glycolysis. *Science*, *305*(5680), 99-103.

Kawano, M., Kumagai, K., Nishijima, M., & Hanada, K. (2006). Efficient trafficking of ceramide from the endoplasmic reticulum to the Golgi apparatus requires a VAMP-associated protein-interacting FFAT motif of CERT. *Journal of Biological Chemistry*, *281*(40), 30279-30288.

Kikuma, K., Li, X., Kim, D., Sutter, D., & Dickman, D. K. (2017). Extended synaptotagmin localizes to presynaptic ER and promotes neurotransmission and synaptic growth in Drosophila. *Genetics*, *207*(3), 993-1006.

Kis, V., Barti, B., Lippai, M., & Sass, M. (2015). Specialized cortex glial cells accumulate lipid droplets in *Drosophila melanogaster*. *PLoS One*, *10*(7), e0131250.

Klein, J. (2000). Membrane breakdown in acute and chronic neurodegeneration: focus on choline-containing phospholipids. *Journal of neural transmission*, *107*, 1027-1063.

Kobayashi, T., & Menon, A. K. (2018). Transbilayer lipid asymmetry. *Current Biology*, *28*(8), R386-R391.

Krahmer, N., Guo, Y., Wilfling, F., Hilger, M., Lingrell, S., Heger, K., ... & Walther, T. C. (2011). Phosphatidylcholine synthesis for lipid droplet expansion is mediated by localized activation of CTP: phosphocholine cytidylyltransferase. *Cell metabolism*, *14*(4), 504-515.

Kremer, M. C., Jung, C., Batelli, S., Rubin, G. M., & Gaul, U. (2017). The glia of the adult *Drosophila* nervous system. *Glia*, *65*(4), 606-638.

Kumagai, K., Yasuda, S., Okemoto, K., Nishijima, M., Kobayashi, S., & Hanada, K. (2005). CERT mediates intermembrane transfer of various molecular species of ceramides. *Journal of Biological Chemistry*, *280*(8), 6488-6495.

Kunduri, G., Turner-Evans, D., Konya, Y., Izumi, Y., Nagashima, K., Lockett, S., ... & Acharya, J. K. (2018). Defective cortex glia plasma membrane structure underlies light-induced epilepsy in cpes mutants. *Proceedings of the National Academy of Sciences*, *115*(38), E8919-E8928.

Lacin, H., Chen, H. M., Long, X., Singer, R. H., Lee, T., & Truman, J. W. (2019). Neurotransmitter identity is acquired in a lineage-restricted manner in the Drosophila CNS. *Elife*, *8*, e43701.

Langfelder, P., & Horvath, S. (2008). WGCNA: an R package for weighted correlation network analysis. *BMC bioinformatics*, *9*(1), 1-13.

Li, L., Tang, X., Taylor, K. G., DuPré, D. B., & Yappert, M. C. (2002). Conformational characterization of ceramides by nuclear magnetic resonance spectroscopy. *Biophysical journal*, *82*(4), 2067-2080.

Liao, Y., Smyth, G. K., & Shi, W. (2014). featureCounts: an efficient general purpose program for assigning sequence reads to genomic features. *Bioinformatics*, *30*(7), 923-930.

Lin, G., Wang, L., Marcogliese, P. C., & Bellen, H. J. (2019). Sphingolipids in the Pathogenesis of Parkinson's Disease and Parkinsonism. *Trends in Endocrinology & Metabolism*, *30*(2), 106-117.

Liu, X., Ma, D., Zhang, Z., Wang, S., Du, S., Deng, X., & Yin, L. (2019). Plant lipid remodeling in response to abiotic stresses. *Environmental and Experimental Botany*, *165*, 174-184.

Liu, L., MacKenzie, K. R., Putluri, N., Maletić-Savatić, M., & Bellen, H. J. (2017). The glia-neuron lactate shuttle and elevated ROS promote lipid synthesis in neurons and lipid droplet accumulation in glia via APOE/D. Cell metabolism, 26(5), 719-737.

Liu, L., Zhang, K., Sandoval, H., Yamamoto, S., Jaiswal, M., Sanz, E., ... & Bellen, H. J. (2015). Glial lipid droplets and ROS induced by mitochondrial defects promote neurodegeneration. *Cell*, *160*(1), 177-190.

Lone, M. A., Aaltonen, M. J., Zidell, A., Pedro, H. F., Saute, J. A. M., Mathew, S., ... & Hornemann, T. (2022). SPTLC1 variants associated with ALS produce distinct sphingolipid signatures through impaired interaction with ORMDL proteins. *The Journal of Clinical Investigation*, *132*(18).

Lone, M. A., Zeng, S., Bourquin, F., Wang, M., Huang, S., Lin, Z., ... & Hornemann, T. (2023). SPTLC1 p. Leu38Arg, a novel mutation associated with childhood ALS. *Biochimica et Biophysica Acta (BBA)-Molecular and Cell Biology of Lipids*, 159359.

Love, M. I., Huber, W., & Anders, S. (2014). Moderated estimation of fold change and dispersion for RNA-seq data with DESeq2. *Genome biology*, *15*(12), 1-21.

Marcus, J., & Popko, B. (2002). Galactolipids are molecular determinants of myelin development and axo–glial organization. *Biochimica et Biophysica Acta (BBA)-General Subjects*, *1573*(3), 406-413.

Marschallinger, J., Iram, T., Zardeneta, M., Lee, S. E., Lehallier, B., Haney, M. S., ... & Wyss-Coray, T. (2020). Lipid-droplet-accumulating microglia represent a dysfunctional and proinflammatory state in the aging brain. *Nature neuroscience*, *23*(2), 194-208.

Marshall, L. L., Stimpson, S. E., Hyland, R., Coorssen, J. R., & Myers, S. J. (2014). Increased lipid droplet accumulation associated with a peripheral sensory neuropathy. *Journal of chemical biology*, *7*, 67-76.

Moessinger, C., Klizaite, K., Steinhagen, A., Philippou-Massier, J., Shevchenko, A., Hoch, M., ... & Thiele, C. (2014). Two different pathways of phosphatidylcholine synthesis, the Kennedy Pathway and the Lands Cycle, differentially regulate cellular triacylglycerol storage. *BMC cell biology*, *15*(1), 1-17.

Moessinger, C., Kuerschner, L., Spandl, J., Shevchenko, A., & Thiele, C. (2011). Human lysophosphatidylcholine acyltransferases 1 and 2 are located in lipid droplets where they catalyze the formation of phosphatidylcholine. *Journal of Biological Chemistry*, *286*(24), 21330-21339.

Molofsky, A. V., Krenick, R., Ullian, E., Tsai, H. H., Deneen, B., Richardson, W. D., ... & Rowitch, D. H. (2012). Astrocytes and disease: a neurodevelopmental perspective. *Genes & development*, *26*(9), 891-907.

Myerowitz, R., Lawson, D., Mizukami, H., Mi, Y., Tifft, C. J., & Proia, R. L. (2002). Molecular pathophysiology in Tay–Sachs and Sandhoff diseases as revealed by gene expression profiling. *Human molecular genetics*, *11*(11), 1343-1351.

Nath, A. S., Parsons, B. D., Makdissi, S., Chilvers, R. L., Mu, Y., Weaver, C. M., ... & Di Cara, F. (2022). Modulation of the cell membrane lipid milieu by peroxisomal β-oxidation induces Rho1 signaling to trigger inflammatory responses. *Cell Reports*, *38*(9).

Nedergaard, M., Ransom, B., & Goldman, S. A. (2003). New roles for astrocytes: redefining the functional architecture of the brain. *Trends in neurosciences*, *26*(10), 523-530.

Nern, A., Pfeiffer, B. D., & Rubin, G. M. (2015). Optimized tools for multicolor stochastic labeling reveal diverse stereotyped cell arrangements in the fly visual system. *Proceedings of the National Academy of Sciences*, *112*(22), E2967-E2976.

Norton, W. T., & Poduslo, S. E. (1973). Myelination in rat brain: changes in myelin composition during brain maturation 1. *Journal of neurochemistry*, *21*(4), 759-773.

O'Brien, J. S. (1965). Stability of the Myelin Membrane: Lipid molecules may impart stability to the myelin membrane through intermolecular cohesion. *Science*, *147*(3662), 1099-1107.

O'Brien, J. S., & Sampson, E. L. (1965). Lipid composition of the normal human brain: gray matter, white matter, and myelin. *Journal of lipid research*, *6*(4), 537-544.

O'Donnell, V. B. (2022). New appreciation for an old pathway: the Lands Cycle moves into new arenas in health and disease. *Biochemical Society Transactions*, *50*(1), 1-11.

Olsen, A. S., & Færgeman, N. J. (2017). Sphingolipids: membrane microdomains in brain development, function and neurological diseases. *Open biology*, *7*(5), 170069.

Osborne, T. F., & Espenshade, P. J. (2009). Evolutionary conservation and adaptation in the mechanism that regulates SREBP action: what a long, strange tRIP it's been. *Genes & development*, *23*(22), 2578-2591.

Pandey, U. B., & Nichols, C. D. (2011). Human disease models in *Drosophila melanogaster* and the role of the fly in therapeutic drug discovery. *Pharmacological reviews*, *63*(2), 411-436.

Pan, X., Dutta, D., Lu, S., & Bellen, H. J. (2023). Sphingolipids in neurodegenerative diseases. *Frontiers in Neuroscience*, *17*, 1137893.

Pant, D. C., Dorboz, I., Schluter, A., Fourcade, S., Launay, N., Joya, J., ... & Pujol, A. (2019). Loss of the sphingolipid desaturase DEGS1 causes hypomyelinating leukodystrophy. *The Journal of clinical investigation*, *129*(3), 1240-1256.

Park, S. Y., Muschalik, N., Chadwick, J., & Munro, S. (2022). *In vivo* characterization of *Drosophila* golgins reveals redundancy and plasticity of vesicle capture at the Golgi apparatus. *Current Biology*, *32*(21), 4549-4564.

Patel, N. H. (1994). Imaging neuronal subsets and other cell types in whole-mount *Drosophila* embryos and larvae using antibody probes. *Methods in cell biology*, *44*, 445-487.

Patro, R., Duggal, G., Love, M. I., Irizarry, R. A., & Kingsford, C. (2017). Salmon provides fast and bias-aware quantification of transcript expression. *Nature methods*, *14*(4), 417-419.

Pettegrew, J. W., Panchalingam, K., Hamilton, R. L., & McClure, R. J. (2001). Brain membrane phospholipid alterations in Alzheimer's disease. *Neurochemical research*, *26*, 771-782.

Pfeiffer, B. D., Ngo, T. T. B., Hibbard, K. L., Murphy, C., Jenett, A., Truman, J. W., & Rubin, G. M. (2010). Refinement of tools for targeted gene expression in Drosophila. *Genetics*, *186*(2), 735-755.

Piccinini, M., Scandroglio, F., Prioni, S., Buccinnà, B., Loberto, N., Aureli, M., ... & Prinetti, A. (2010). Deregulated sphingolipid metabolism and membrane organization in neurodegenerative disorders. *Molecular neurobiology*, *41*, 314-340.

Plongthongkum, N., Kullawong, N., Panyim, S., & Tirasophon, W. (2007). Ire1 regulated XBP1 mRNA splicing is essential for the unfolded protein response (UPR) in *Drosophila melanogaster*. *Biochemical and biophysical research communications*, *354*(3), 789-794.

Poitelon, Y., Kopec, A. M., & Belin, S. (2020). Myelin fat facts: an overview of lipids and fatty acid metabolism. *Cells*, *9*(4), 812.

Qin, J., Berdyshev, E., Goya, J., Natarajan, V., & Dawson, G. (2010). Neurons and oligodendrocytes recycle sphingosine 1-phosphate to ceramide: significance for apoptosis and multiple sclerosis. *Journal of Biological Chemistry*, *285*(19), 14134-14143.

Renuart, A. W. (1966). Screening for inborn errors of metabolism associated with mental deficiency or neurologic disorders or both. *New England Journal of Medicine*, *274*(7), 384-387.

Riedel, F., Gillingham, A. K., Rosa-Ferreira, C., Galindo, A., & Munro, S. (2016). An antibody toolkit for the study of membrane traffic in *Drosophila melanogaster*. *Biology open*, *5*(7), 987-992.

Ryoo, H. D., Domingos, P. M., Kang, M. J., & Steller, H. (2007). Unfolded protein response in a *Drosophila* model for retinal degeneration. *The EMBO journal*, *26*(1), 242-252.

Sarov, M., Barz, C., Jambor, H., Hein, M. Y., Schmied, C., Suchold, D., ... & Schnorrer, F. (2016). A genome-wide resource for the analysis of protein localisation in *Drosophila*. *elife*, *5*, e12068.

Schmitt, S., Castelvetri, L. C., & Simons, M. (2015). Metabolism and functions of lipids in myelin. *Biochimica et Biophysica Acta (BBA)-Molecular and Cell Biology of Lipids*, *1851*(8), 999-1005.

Schönfeld, P., & Reiser, G. (2013). Why does brain metabolism not favor burning of fatty acids to provide energy?-Reflections on disadvantages of the use of free fatty acids as fuel for brain. *Journal of Cerebral Blood Flow & Metabolism*, *33*(10), 1493-1499.

Schuck, S., Prinz, W. A., Thorn, K. S., Voss, C., & Walter, P. (2009). Membrane expansion alleviates endoplasmic reticulum stress independently of the unfolded protein response. *Journal of Cell Biology*, *187*(4), 525-536.

Sidransky, E., & Lopez, G. (2012). The link between the GBA gene and parkinsonism. *The Lancet Neurology*, *11*(11), 986-998.

Sidransky, E., Nalls, M. A., Aasly, J. O., Aharon-Peretz, J., Annesi, G., Barbosa, E. R., ... & Ziegler, S. G. (2009). Multicenter analysis of glucocerebrosidase mutations in Parkinson's disease. *New England Journal of Medicine*, *361*(17), 1651-1661.

Simons, M., & Nave, K. A. (2016). Oligodendrocytes: myelination and axonal support. *Cold Spring Harbor perspectives in biology*, *8*(1), a020479.

Southall, T. D., Gold, K. S., Egger, B., Davidson, C. M., Caygill, E. E., Marshall, O. J., & Brand, A. H. (2013). Cell-type-specific profiling of gene expression and chromatin binding without cell isolation: assaying RNA Pol II occupancy in neural stem cells. *Developmental cell*, *26*(1), 101-112.

Sriburi, R., Bommiasamy, H., Buldak, G. L., Robbins, G. R., Frank, M., Jackowski, S., & Brewer, J. W. (2007). Coordinate regulation of phospholipid biosynthesis and secretory pathway gene expression in XBP-1 (S)-induced endoplasmic reticulum biogenesis. *Journal of Biological Chemistry*, *282*(10), 7024-7034.

Su, X., Lu, W., & Rabinowitz, J. D. (2017). Metabolite spectral accuracy on orbitraps. *Analytical chemistry*, *89*(11), 5940-5948.

Syeda, S. B., Lone, M. A., Mohassel, P., Donkervoort, S., Munot, P., França, M. C., ... & Bönnemann, C. G. (2023). Recurrent de novo SPTLC2 variant causes childhood-onset amyotrophic lateral sclerosis (ALS) by excess sphingolipid synthesis. *Journal of Neurology, Neurosurgery & Psychiatry*.

Truman, J. W., Schuppe, H., Shepherd, D., & Williams, D. W. (2004). Developmental architecture of adult-specific lineages in the ventral CNS of *Drosophila*.

Tsacopoulos, M., & Magistretti, P. J. (1996). Metabolic coupling between glia and neurons. *The Journal of neuroscience*, *16*(3), 877.

Tzou, F. Y., Su, T. Y., Lin, W. S., Kuo, H. C., Yu, Y. L., Yeh, Y. H., ... & Chan, C. C. (2021). Dihydroceramide desaturase regulates the compartmentalization of Rac1 for neuronal oxidative stress. *Cell reports*, *35*(2).

Ugur, B., Chen, K., & Bellen, H. J. (2016). *Drosophila* tools and assays for the study of human diseases. *Disease models & mechanisms*, *9*(3), 235-244.

Vacaru, A. M., van den Dikkenberg, J., Ternes, P., & Holthuis, J. C. (2013). Ceramide Phosphoethanolamine Biosynthesis in *Drosophila* Is Mediated by a Unique Ethanolamine Phosphotransferase in the Golgi Lumen. *Journal of Biological Chemistry*, *288*(16), 11520-11530.

Vance, J. E., & Tasseva, G. (2013). Formation and function of phosphatidylserine and phosphatidylethanolamine in mammalian cells. *Biochimica et Biophysica Acta (BBA)-Molecular and Cell Biology of Lipids*, *1831*(3), 543-554.

Vieira, C. R., Munoz-Olaya, J. M., Sot, J., Jiménez-Baranda, S., Izquierdo-Useros, N., Abad, J. L., ... & Goñi, F. M. (2010). Dihydrosphingomyelin impairs HIV-1 infection by rigidifying liquid-ordered membrane domains. *Chemistry & biology*, *17*(7), 766-775.

Volkenhoff, A., Weiler, A., Letzel, M., Stehling, M., Klämbt, C., & Schirmeier, S. (2015). Glial glycolysis is essential for neuronal survival in Drosophila. *Cell metabolism*, *22*(3), 437-447.

Wang, G., & Bieberich, E. (2018). Sphingolipids in neurodegeneration (with focus on ceramide and S1P). *Advances in biological regulation*, *70*, 51-64.

Wang, L., Lin, G., Zuo, Z., Li, Y., Byeon, S. K., Pandey, A., & Bellen, H. J. (2022). Neuronal activity induces glucosylceramide that is secreted via exosomes for lysosomal degradation in glia. *Science Advances*, *8*(28), eabn3326.

Wenger, D. A., Rafi, M. A., Luzi, P., Datto, J., & Costantino-Ceccarini, E. (2000). Krabbe disease: genetic aspects and progress toward therapy. *Molecular genetics and metabolism*, *70*(1), 1-9.

Wolf, N. I., Ffrench-Constant, C., & van der Knaap, M. S. (2021). Hypomyelinating leukodystrophies—Unravelling myelin biology. *Nature Reviews Neurology*, *17*(2), 88-103.

Wu, Chen-Yi, Jhih-Gang Jhang, Wan-Syuan Lin, Pei-Huan Chuang, Chih-Wei Lin, Li-An Chu, Ann-Shyn Chiang, Han-Chen Ho, Chih-Chiang Chan, and Shu-Yi Huang. "Dihydroceramide desaturase promotes the formation of intraluminal vesicles and inhibits autophagy to increase exosome production." *Iscience* 24, no. 12 (2021).

Yang, S. Y., He, X. Y., & Schulz, H. (1987). Fatty acid oxidation in rat brain is limited by the low activity of 3-ketoacyl-coenzyme A thiolase. *Journal of Biological Chemistry*, *262*(27), 13027-13032.

Yildirim, K., Petri, J., Kottmeier, R., & Klämbt, C. (2019). Drosophila glia: Few cell types and many conserved functions. *Glia*, *67*(1), 5-26.

Ziegler, A. B., Brüsselbach, F., & Hovemann, B. T. (2013). Activity and coexpression of Drosophila black with ebony in fly optic lobes reveals putative cooperative tasks in vision that evade electroretinographic detection. *Journal of Comparative Neurology*, *521*(6), 1207-1224.

Figure legends

Figure 1. *ifc* regulates CNS and glial morphology. a) Ventral views of late-third instar larvae of indicated genotype showing 3xP3 RFP labeling of CNS and nerves. Arrowheads indicate nerve bulges; scale bar is 200µm. b-b') Schematic of Ifc (b) and human DEGS1 (b') proteins indicating location and nature of *ifc* mutations and 15 HLD-18-causing *DEGS1* mutations in humans (Karsai et al. 2019; Pant et al. 2019; Dolgin et al. 2019). c) Schematic of *de novo* ceramide biosynthesis pathway indicating the subcellular location of ceramide synthesis and ceramide modifications. d)

Chemical structure of dihydroceramide and ceramide; arrow indicates *trans* carbon-carbon double bond between C4 and C5 in the sphingoid backbone created by the enzymatic action of Ifc/DEGS1. e) Normalized quantification of the relative levels of dihydroceramide, ceramide, and six related sphingolipid species in the dissected CNS of wild-type and *ifc*$^{-/-}$ late-third instar larvae. f) Ventral views of *Drosophila* CNS and peripheral nerves in wild-type and *ifc*$^{-/-}$ mutant late-third instar larvae labeled for NCAD to mark the neuropil, HRP to label axons, RFP to label glia, DPN to label neuroblasts, ELAV to label neurons, and FABP to label cortex glia. Anterior is up for images; scale bar is 100μm for whole CNS images and 20μm for peripheral nerve image. Statistics: * denotes $p < 0.05$, ** denotes $p < 0.01$, *** denotes $p < 0.001$, **** *denotes* $p < 0.0001$.

Figure 2. Loss of *ifc* disrupts glial morphology. a-e') High magnification ventral views as well as X-Z and Y-Z projections of the ventral nerve cord of wildtype and *ifc*$^{-/-}$ late third instar larvae labeled for ELAV (red) for neurons and Myr-GFP (green) for cell membranes of indicated glial subtype. Anterior is up; scale bar is 40 μm. f-j') High magnification views of individual glial cells for the indicated glial subtype in the ventral nerve cord of wild-type and *ifc*$^{-/-}$ larvae generated by the MultiColor FlpOut method (Nern et al. 2015). Anterior is up; scale bar is 20 μm. k-n) Quantification of total number of indicated glial subtype in the ventral nerve cord of wild-type and *ifc*$^{-/-}$ late third instar larvae (n = 7 for k, l, n; n = 6 for m). Statistics: * denotes $p < 0.05$, **** denotes $p < 0.0001$, and ns, not significant.

Figure 3. *ifc* acts in glia to regulate CNS structure and glial morphology. a-i) Ventral views of photomontages of the CNS of late third instar larvae labeled for FABP (greyscale) to mark cortex glia in late third instar larvae of indicated genotype. Neuronal-specific transgene expression was achieved by using *ELAV-GAL4* combined with *REPO-GAL80*; glial-specific transgene expression was achieved by using REPO-GAL4. j-k) Quantification of the number of swollen cortex glia in

the abdominal segments of the CNS of late-third instar larvae of the indicated genotype for the RNAi (j) and gene rescue assays (k). Statistics: * denotes $p < 0.05$, ** denotes $p < 0.01$, *** denotes $p < 0.001$, **** denotes $p < 0.0001$, and ns, not significant.

Figure 4. *ifc* is predominately expressed in glia in the larval CNS. Dorsal (a-d) and ventral (e-g) views of the CNS of late-third instar wild-type larvae labeled for *ifc* RNA (grey in a; red in b), *ifc-GAL4>nRFP* (red, c-g), EBONY to mark astrocytes (green, b-c), ELAV to mark neurons (green, d, g), and REPO to mark glia (green, e-f). Panels e and f show surface and interior views, respectively, to highlight primarily the surface glia (e) and cortex glia (f). Arrowheads in d and g identify neurons with low level *ifc-GAL4* expression. Anterior is up; scale bar is 100μm for panel 'a' and 30μm for panels 'b-g'.

Figure 5. Ifc localizes to the ER and regulates ER morphology. (a-h) High magnification ventral views of abdominal segments in the CNS of wild-type (a-h) and $ifc^{-/-}$ (e'-h') late third instar larvae labeled for RFP (green, a-h'), Cnx99A (red, a e, e'), ESYT (red, b), Gogin 84 (red, c, f, f'), Golgin 285 (Red, d, g, g'), and LAMP (red, h, h'). Anterior is up; scale bar is 30μm.

Figure 6. Loss of *ifc* leads to internal membrane accumulation and lipid droplet loss in cortex glia. a-e') TEM images of cortex glia cell body (a-b') and neuronal cell bodies (c-d') at low (a-a') and high (b-d') magnifications in the ventral nerve cord of wild-type (a-d) and $ifc^{-/-}$ (a'-e') late third instar larvae. (a-a') Dotted lines demarcate cell boundary of cortex glia; yellow squares highlight regions magnified in b, b', e'. Scale bar is 3μm for a and a' and 1μm for b-b'. (b-b') Cy denotes cytoplasm; Nu denotes nucleus. Solid white arrows highlight the layered internal membranes that occupy the cytoplasm of $ifc^{-/-}$ cortex glia. (c-d') Black arrows highlight the cortex glia membrane extensions

that fully enwrap neuronal cell bodies; hollow white arrows denote the absence of cortex glia membrane extensions; white asterisk denotes lipid droplets. Scale bar is 2μm. e-e') Additional example of cortex glia cell body in *ifc*$^{-/-}$ larvae with layered internal membranes. Scale bar is 2μm for e and 1μm for e'. f) Cortex glia in *ifc* mutant larvae labeled for Myr-GFP (green) to label membranes and Cnx99A to label ER membranes. Scale bar is 30μm. g-h) Black and white and colored TEM cross-sections of peripheral nerves in wild type and *ifc*$^{-/-}$ late-third instar larvae. Blue marks perineurial glia; purple marks subperineurial glia; pink marks wrapping glia. Scale bar is 2μm. i-i') High magnification ventral views of abdominal segments in the ventral nerve cord of wild-type (i) and *ifc* mutant (i') third instar larvae labeled for BODIPY (green) to mark lipid droplets and FABP (red) to label cortex glia. Anterior is up; scale bar is 30μm. j) Graph of log-fold change in the transcription of five genes that promote membrane lipid synthesis in *ifc*$^{-/-}$ larvae relative to wild type. k-m) Quantification of the number (g) and area of lipid droplets (h, i) in the dissected CNS of wild-type and *ifc*$^{-/-}$ larvae. Statistics: * denotes $p < 0.05$, ** denotes $p < 0.01$, *** denotes $p < 0.001$, **** denotes $p < 0.0001$, and ns, not significant.

Figure 7. PC, PE, PS, and TG exhibit higher saturation profiles in a CNS-specific manner in *ifc* mutant late third instar larvae. a-c). Quantification of total (a) and species-specific (b-c) TGs in the whole larvae (a, c) and dissected CNS (a-c) of wild-type and *ifc*$^{-/-}$ larvae. d-f). Quantification of total (d) and species-specific (e-f) PCs in the whole larvae (d, f) and dissected CNS (d-f) of wild-type and *ifc*$^{-/-}$ larvae. g-i). Quantification of total (g) and species-specific (h-i) PEs in the whole larvae (g-h) and dissected CNS (g-i) of wild-type and *ifc*$^{-/-}$ larvae. j-l). Quantification of total (j) and species-specific (k-l) PSs in the whole larvae (j, l) and dissected CNS (j-l) of wild-type and *ifc*$^{-/-}$ larvae. Statistics: * denotes $p < 0.05$, ** denotes $p < 0.01$, *** denotes $p < 0.001$, **** denotes $p < 0.0001$, and ns, not significant.

Figure 8. Reduction of *schlank* function suppresses the *ifc* CNS phenotype. a-b). Quantification of CNS elongation (a) and 3xP3 RFP intensity (b) in *ifc* mutants alone, *ifc* mutants heterozygous for the *schlank[G0365]* loss-of-function allele, or *ifc* mutants in which *schlank* function is reduced via RNAi in glial cells. c-d). Quantification of the area (c) and number (d) of lipid droplets in the dissected CNS of *ifc* mutants and *ifc* mutants in which *schlank* function is reduced via RNAi in glial cells. e-h). TEM images of cortex glia cell body (e-f) and neuronal cell bodies (g-h) at low (e) and high (f-h) magnifications in the ventral nerve cord of $ifc^{-/-}$; *repo>schlank RNAi* late third instar larvae. Dotted lines demarcate cell boundary of cortex glia; yellow squares highlight regions magnified in b. Scale bar is 3μm for e, 1μm for f, and 2μm for g-h. (d) Cy denotes cytoplasm; Nu denotes nucleus. (g-h) Black asterisk denotes lipid droplets. i-j). Ventral views of abdominal sections of the CNS of $ifc^{-/-}$; *UAS-schlank RNAi/+* larvae (i) and $ifc^{-/-}$; repoGAL4/*UAS-schlank RNAi* larvae (j) labeled for neurons (ELAV, Green) and cortex glia (FABP, red/grey). Anterior is up; scale bar is 50 μm. Statistics: * denotes $p < 0.05$, ** denotes $p < 0.01$, *** denotes $p < 0.001$, **** denotes $p < 0.0001$, and ns, not significant.

Figure 1.

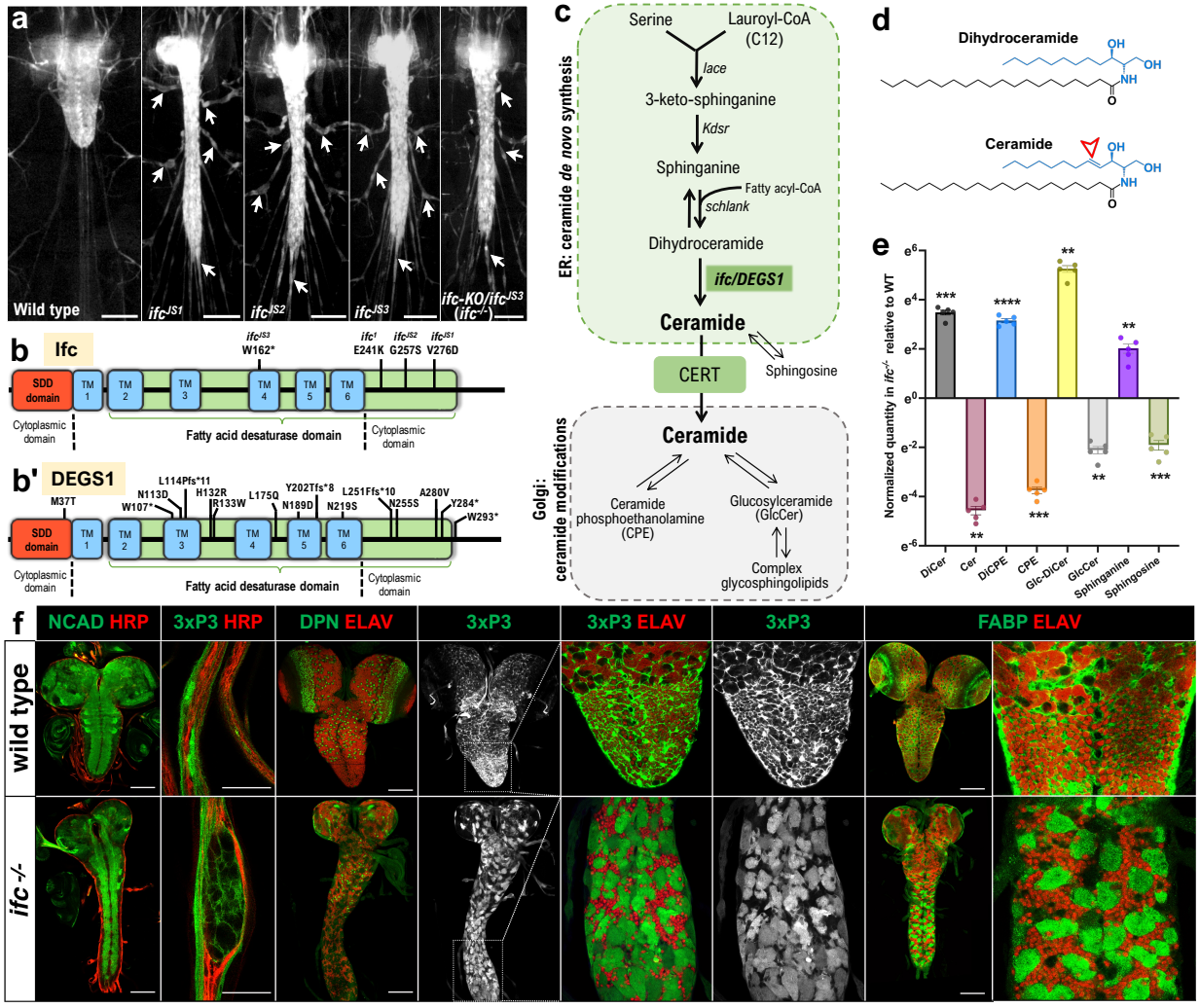
a
Wild type
ifc^JS1
ifc^JS2
ifc^JS3
ifc-KO/ifc^JS3 (ifc^-/-)
b
Ifc
SDD domain
TM 1
TM 2
TM 3
TM 4
TM 5
TM 6
ifc^JS3 W162*
ifc^1 E241K
ifc^JS2 G257S
ifc^JS1 V276D
Cytoplasmic domain
Fatty acid desaturase domain
Cytoplasmic domain
b'
DEGS1
M37T
W107*
N113D
L114Pfs*11
H132R
R133W
L175Q
Y202Tfs*8
N189D
N219S
L251Ffs*10
N255S
A280V
Y284*
W293*
c
ER: ceramide de novo synthesis
Serine
Lauroyl-CoA (C12)
lace
3-keto-sphinganine
Kdsr
Sphinganine
Fatty acyl-CoA
schlank
Dihydroceramide
ifc/DEGS1
Ceramide
CERT
Sphingosine
Golgi: ceramide modifications
Ceramide
Ceramide phosphoethanolamine (CPE)
Glucosylceramide (GlcCer)
Complex glycosphingolipids
d
Dihydroceramide
Ceramide
OH
NH
O
e
Normalized quantity in ifc^-/- relative to WT
DiCer
Cer
DiCPE
CPE
Glc-DiCer
GlcCer
Sphinganine
Sphingosine
f
NCAD HRP
3xP3 HRP
DPN ELAV
3xP3
3xP3 ELAV
3xP3
FABP ELAV
wild type
ifc -/-

Figure 2.

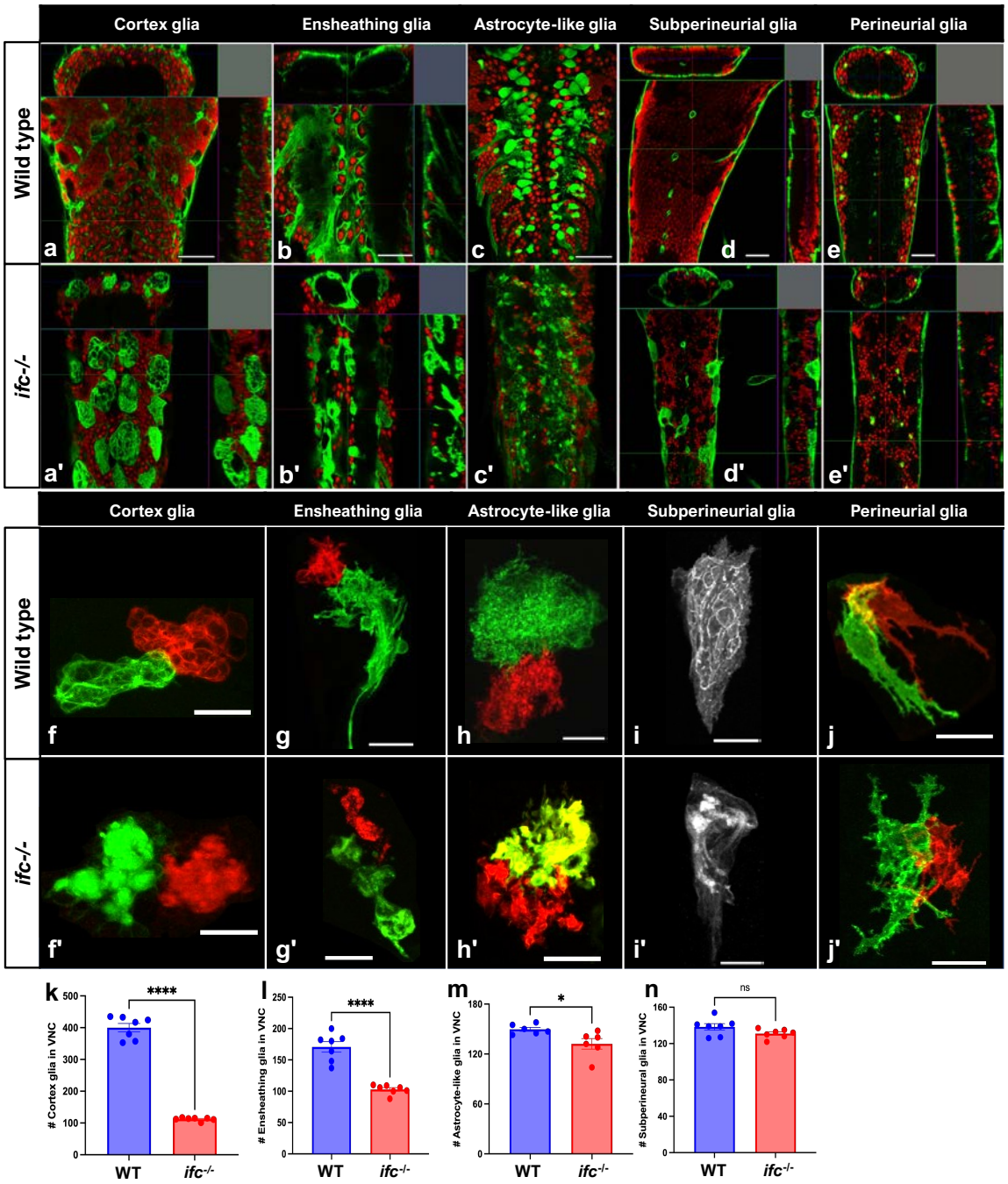
Cortex glia
Ensheathing glia
Astrocyte-like glia
Subperineurial glia
Perineurial glia
Wild type
ifc-/-
a
b
c
d
e
a'
b'
c'
d'
e'
f
g
h
i
j
f'
g'
h'
i'
j'
k
l
m
n
****
****
*
ns
Cortex glia in VNC
Ensheathing glia in VNC
Astrocyte-like glia in VNC
Subperineural glia in VNC
WT
ifc-/-

Figure 3.

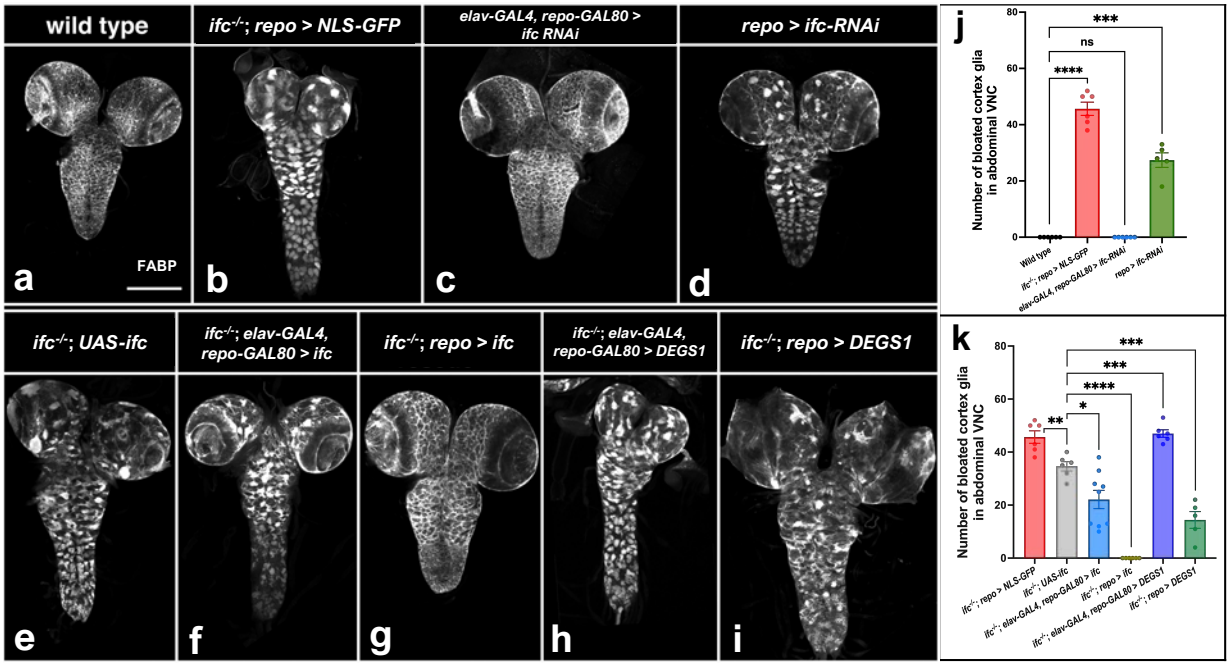

Figure 4.

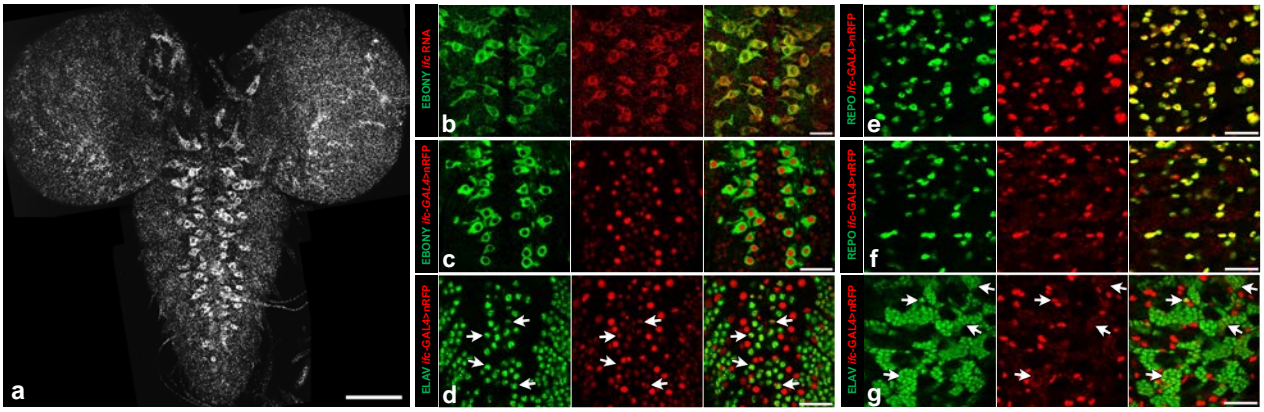

Figure 5.

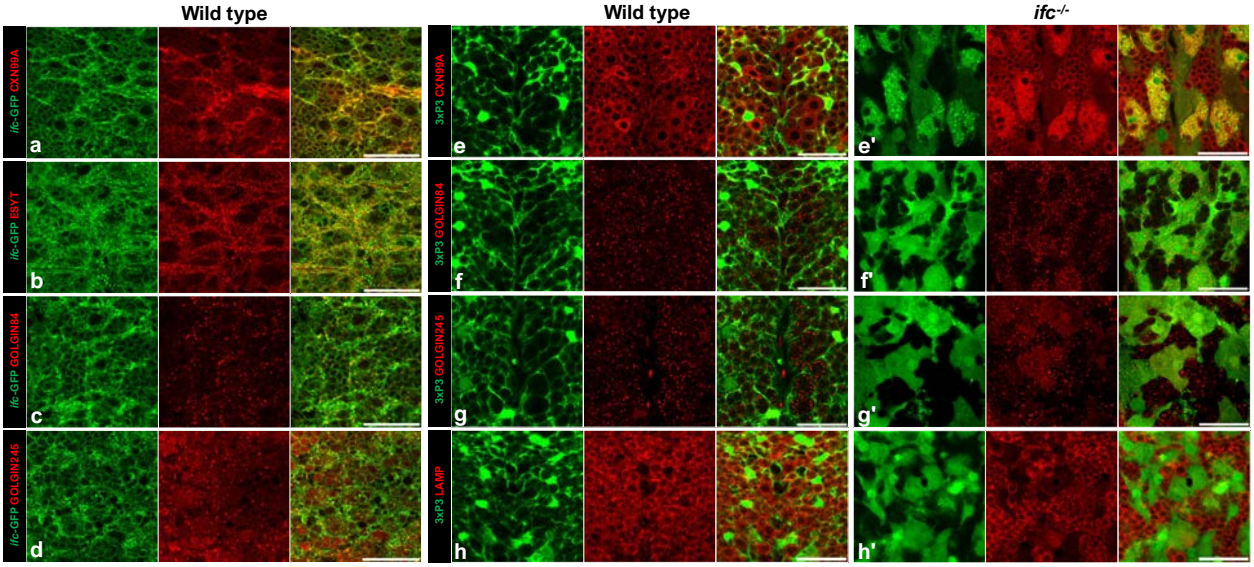
Wild type
Wild type
ifc-/-
ifc-GFP CXN99A
ifc-GFP ESYT
ifc-GFP GOLGIN84
ifc-GFP GOLGIN245
3xP3 CXN99A
3xP3 GOLGIN84
3xP3 GOLGIN245
3xP3 LAMP
a
b
c
d
e
f
g
h
e'
f'
g'
h'

Figure 6.

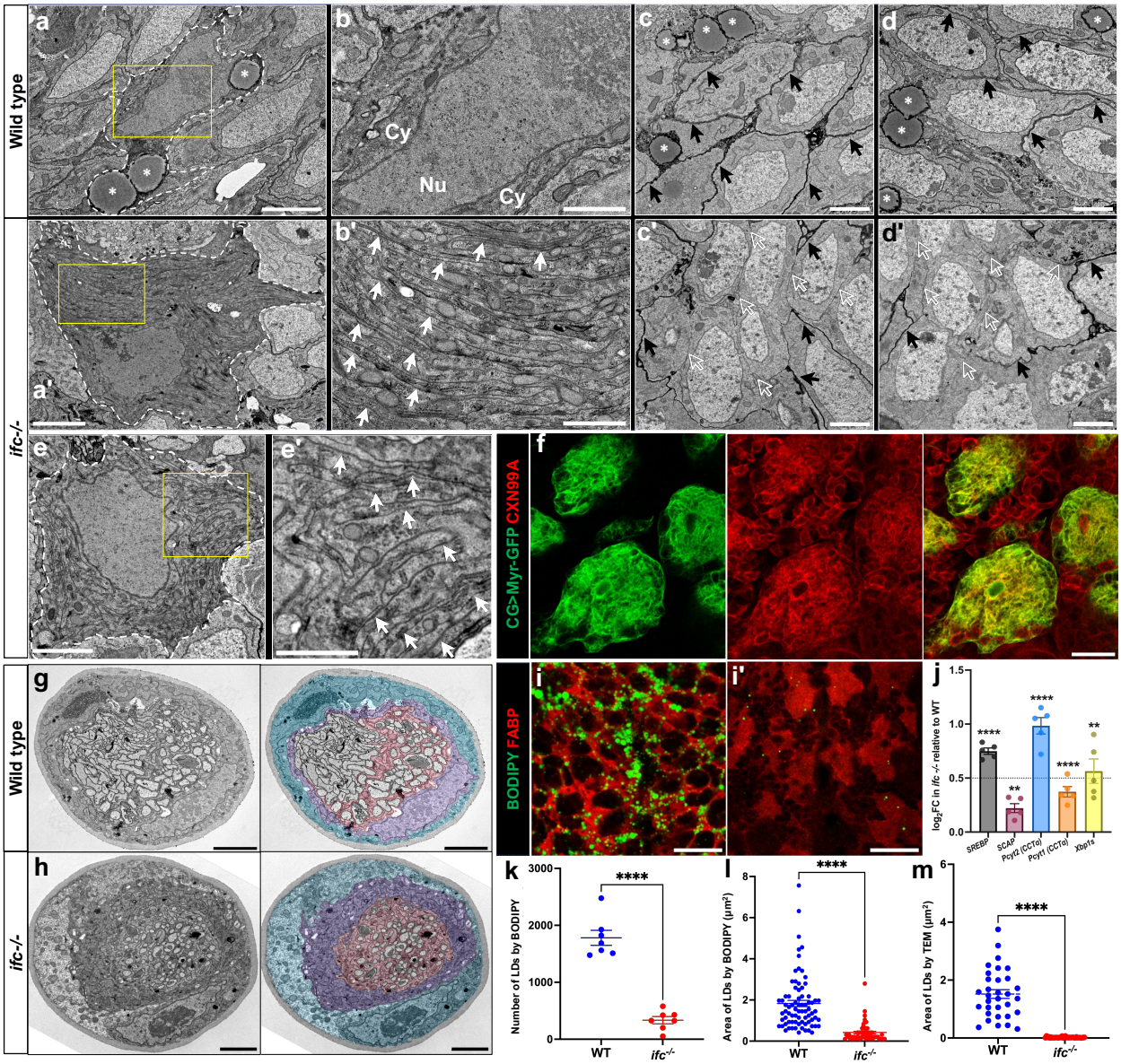
Wild type
ifc-/-
a
b
c
d
a'
b'
c'
d'
Cy
Nu
Cy
e
e'
f
CG>Myr-GFP CXN99A
g
h
i
i'
BODIPY FABP
j
log2FC in ifc-/- relative to WT
SREBP
SCAP
Pcyt2 (CCTα)
Pcyt1 (CCTα)
Xbp1s
k
Number of LDs by BODIPY
l
Area of LDs by BODIPY (μm²)
m
Area of LDs by TEM (μm²)
WT
ifc-/-
****

Figure 7.

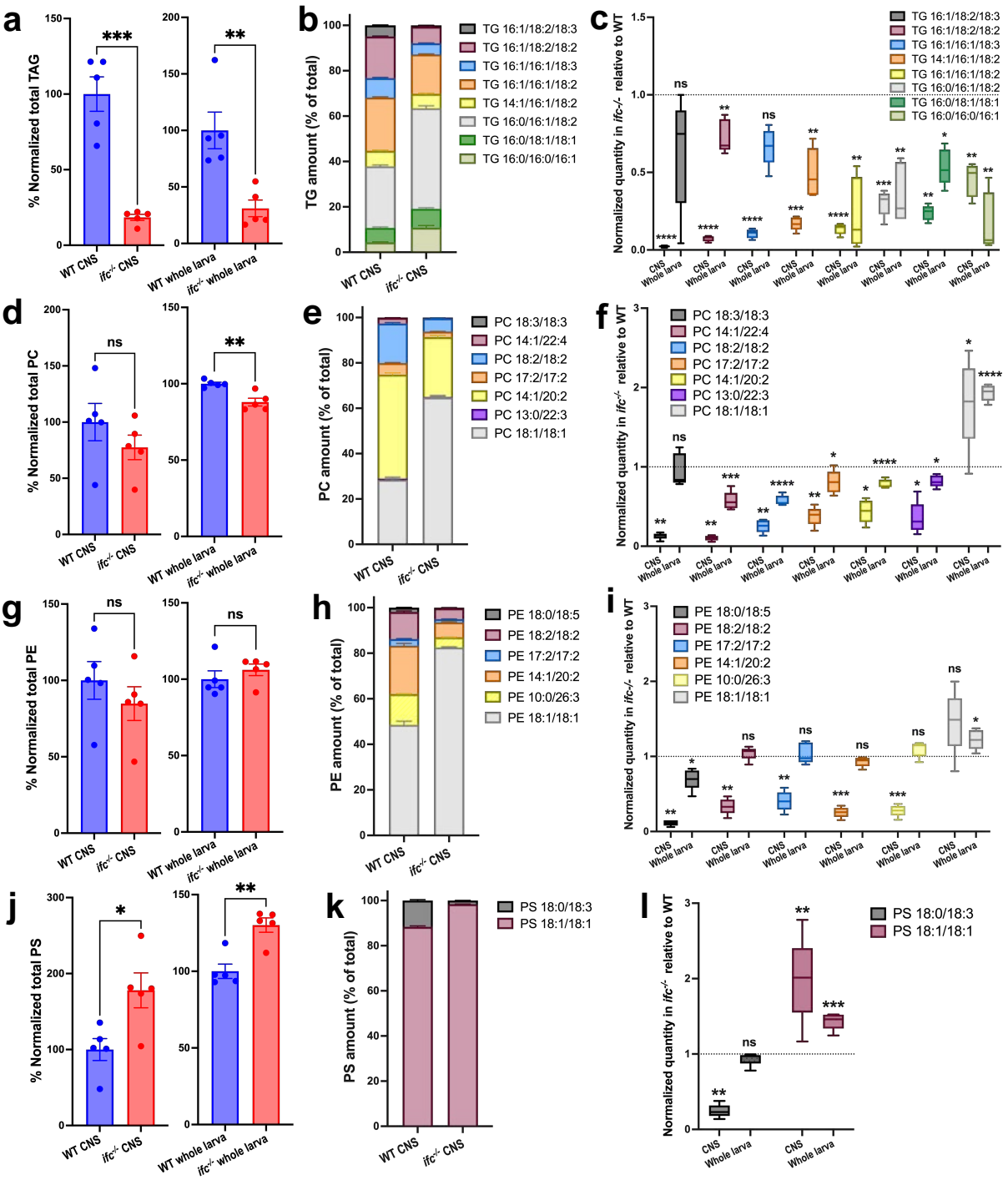
a
% Normalized total TAG
WT CNS
ifc-/- CNS
WT whole larva
ifc-/- whole larva
b
TG amount (% of total)
TG 16:1/18:2/18:3
TG 16:1/18:2/18:2
TG 16:1/16:1/18:3
TG 16:1/16:1/18:2
TG 14:1/16:1/18:2
TG 16:0/16:1/18:2
TG 16:0/18:1/18:1
TG 16:0/16:0/16:1
c
Normalized quantity in ifc-/- relative to WT
CNS
Whole larva
d
% Normalized total PC
e
PC amount (% of total)
PC 18:3/18:3
PC 14:1/22:4
PC 18:2/18:2
PC 17:2/17:2
PC 14:1/20:2
PC 13:0/22:3
PC 18:1/18:1
f
g
% Normalized total PE
h
PE amount (% of total)
PE 18:0/18:5
PE 18:2/18:2
PE 17:2/17:2
PE 14:1/20:2
PE 10:0/26:3
PE 18:1/18:1
i
j
% Normalized total PS
k
PS amount (% of total)
PS 18:0/18:3
PS 18:1/18:1
l

Figure 8.

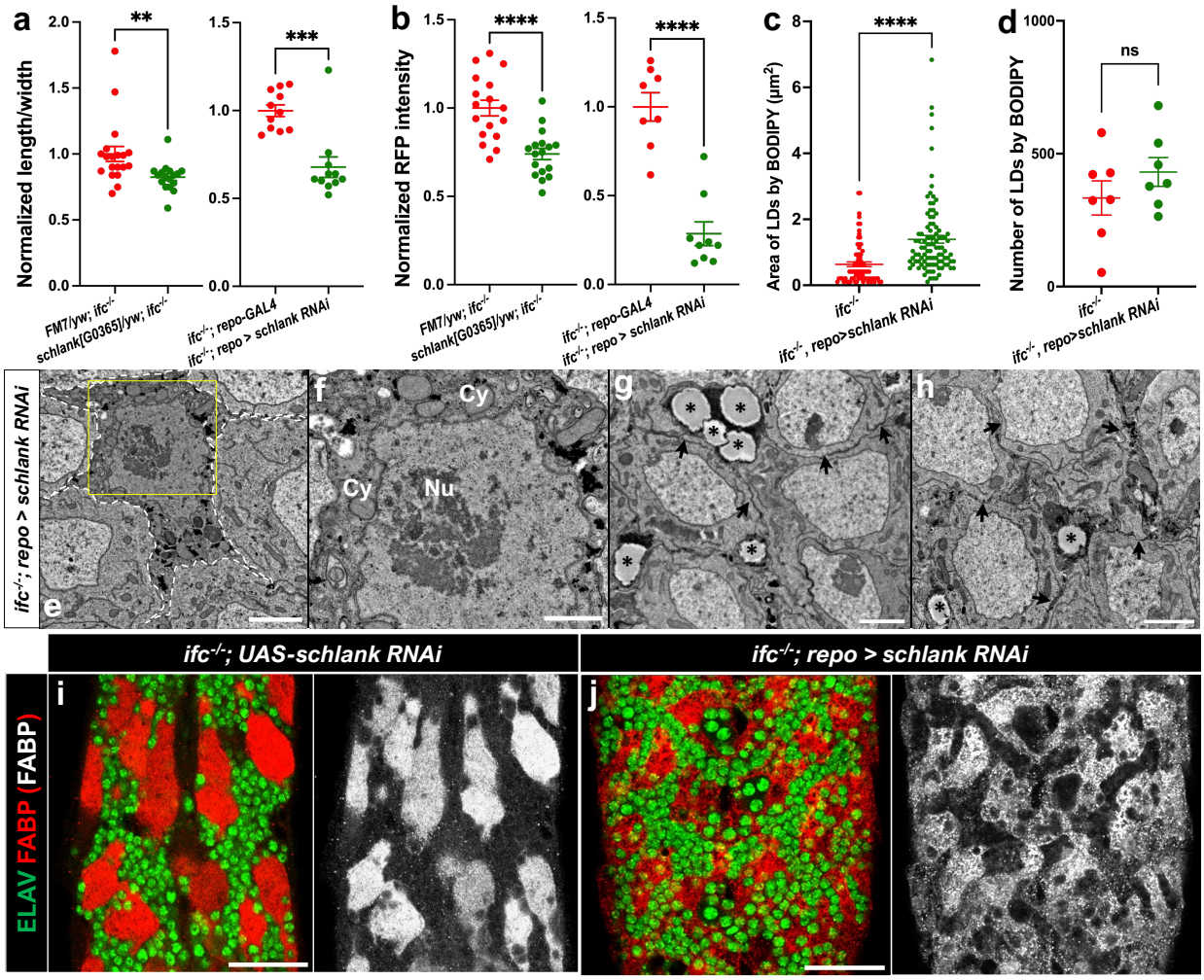
a
Normalized length/width
**
***
FM7/yw; ifc-/-
schlank[G0365]/yw; ifc-/-
ifc-/-; repo-GAL4
ifc-/-; repo > schlank RNAi
b
Normalized RFP intensity
****
****
FM7/yw; ifc-/-
schlank[G0365]/yw; ifc-/-
ifc-/-; repo-GAL4
ifc-/-; repo > schlank RNAi
c
Area of LDs by BODIPY (µm2)
****
ifc-/-
ifc-/- , repo>schlank RNAi
d
Number of LDs by BODIPY
ns
ifc-/-
ifc-/- , repo>schlank RNAi
ifc-/-; repo > schlank RNAi
e
f
Cy
Cy
Nu
g
h
ifc-/-; UAS-schlank RNAi
ifc-/-; repo > schlank RNAi
ELAV FABP (FABP)
i
j